The Astrophysical Journal, 811:24 (18pp), 2015 September 20 doi:10.1088/0004-637X/811/1/24

CHARACTERIZATION OF THE INNER KNOT OF THE CRAB: THE SITE OF THE GAMMA-RAY FLARES?

Alexander Rudy[1], Dieter Horns[2], Andrea DeLuca[3,4], Jeffery Kolodziejczak[5], Allyn Tennant[5], Yajie Yuan[6], Rolf Buehler[7], Jonathon Arons[8], Roger Blandford[6], Patrizia Caraveo[3,4], Enrico Costa[9], Stephan Funk[6], Elizabeth Hays[10], Andrei Lobanov[11], Claire Max[1], Michael Mayer[7], Roberto Mignani[3,12], Stephen L. O'Dell[5], Roger Romani[6], Marco Tavani[3,4], and Martin C. Weisskopf[5]

[1] Department of Astronomy & Astrophysics, University of California, Santa Cruz, CA 95064, USA
[2] Institut für Experimentalphysik, Universität Hamburg, Luruper Chaussee 149, D-22761 Hamburg, Germany
[3] INAF–IASF Milano, via E. Bassini 15, I-20133 Milano, Italy
[4] INFN Pavia, via A. Bassi 6, I-27100 Pavia, Italy
[5] NASA Marshall Space Flight Center, Astrophysics Office (ZP12), Huntsville, AL 35812, USA
[6] W. W. Hansen Experimental Physics Laboratory, Kavli Institute for Particle Astrophysics and Cosmology, Stanford University, Stanford, CA 94305, USA
[7] DESY, Platanenallee 6, D-15738 Zeuthen, Germany
[8] Astronomy Department and Theoretical Astrophysics Center, University of California, Berkeley, 601 Campbell Hall, Berkeley, CA 94720, USA
[9] INFN Roma Tor Vergata, via della Ricerca Scientifica 1, I-00133 Roma, Italy
[10] NASA Goddard Space Flight Center, Astrophysics Science Division, Greenbelt, MD 20771, USA
[11] Max-Planck-Institut für Radioastronomie, auf dem Hügel 69, D-53121 Bonn, Germany
[12] Kepler Institute of Astronomy, University of Zielona Gora, Lubuska 2, 65-265 Zielona Gora, Poland
Received 2015 April 17; accepted 2015 August 3; published 2015 September 16

ABSTRACT

A particularly intriguing recent result from γ-ray astronomy missions is the detection of powerful flares from the Crab Nebula, which challenges the current understanding of pulsar wind nebulae and acceleration mechanisms. To search for the production site(s) of these flares, we conducted a multi-wavelength observing campaign using Keck, the *Hubble Space Telescope* (*HST*), and the *Chandra X-ray Observatory*. As the short timescales of the γ-ray flares ($\lesssim$1 day) suggest a small emitting region, the Crab's inner knot (about 0.6 arcsec from the pulsar) is a candidate site for such flaring. This paper describes observations of the inner knot, seeking to understand its nature and possible relationship with γ-ray flares. Using singular-value decomposition, analysis of the *HST* images yielded results consistent with traditional methods while substantially reducing some uncertainties. These analyses show that the knot's intrinsic properties (especially size and brightness) are correlated with its (projected) separation from the pulsar. This characterization of the inner knot helps in constraining standard shock model parameters, under the assumption that the knot lies near the shocked surface. While the standard shock model gives good agreement in several respects, two puzzles persist: (a) the observed angular size of the knot relative to the pulsar–knot separation is much smaller than expected; and (b) the variable high degree of polarization (reported by others) is difficult to reconcile with a highly relativistic downstream flow. However, the IR–optical flux of the inner knot is marginally consistent with the shock accelerating most of the Nebula's optical-emitting particles.

Key words: ISM: jets and outflows – ISM: supernova remnants – pulsars: individual (Crab) – techniques: image processing

1. INTRODUCTION

The Crab pulsar and its nebula are one of the most studied targets in the sky at all wavelengths. It serves as a test bed for pulsar theories as well as, more generally, for astrophysical non-thermal processes. A very thorough review of the Crab system, including high spatial resolution observations with *Hubble Space Telescope* (*HST*) and *Chandra*, showing the complex, dynamic interaction of the pulsar wind with the surrounding medium, has been compiled by Hester (2008). A more recent review by Bühler & Blandford (2014) also includes the saga of the γ-ray flares.

A crucial question implied by the observations of the γ-ray flares is "how are the particles being accelerated to sustain the flaring behavior?" Radiating particles must have PeV energies to emit synchrotron radiation at the observed γ-ray wavelengths. A mechanism is needed that can accelerate particles to such high energies in less than one gyration time in the ambient magnetic field. For example, the large flare of 2011 April produced a radiant energy equivalent to the energy stored in the mean magnetic field within a region of order 2×10^{14} m subtending an angle $\approx 0\farcs3$ at 2 kpc, consistent with the emission-region size estimated from light travel time arguments (Weisskopf et al. 2013).

An intense theoretical effort is underway to explain the variable Crab behaviors (e.g., Komissarov & Lyutikov 2011; Uzdensky et al. 2011; Yuan et al. 2011; Arons 2012; Bykov et al. 2012; Cerutti et al. 2012, 2013; Clausen-Brown & Lyutikov 2012; Lyubarsky 2012; Lyutikov et al. 2012; Sturrock & Aschwanden 2012; Baty et al. 2013; Teraki & Takahara 2013). However, the mechanism driving the flares, their impulsive nature, the $\approx$12-month recurrence time, and the location remain unknown. Possible explanations include plasma instabilities in the nebula, magnetic reconnection, discontinuity in the pulsar wind acceleration, emission from the anvil, emission from the inner knot, or portions of the termination shock. See, for example, the review by Hester (2008) for the association of specific features with this nomenclature.

There are a number of reasons to suspect that the feature known as the "inner knot" should be considered as a possible site for the origin of the flares (e.g., Komissarov & Lyutikov 2011). First, the luminosity of the flares accounts for a relatively high fraction of the pulsar spin-down luminosity

(assuming a radiation efficiency of 3%–5%), suggesting an origin in a region close to the pulsar (Tavani et al. 2011). Second, the very short variability timescales combined with causality arguments, strongly constrain the size of the flare's emitting region (Striani et al. 2011; Buehler et al. 2012).

A multi-wavelength campaign to study the Crab, described in Weisskopf et al. (2013), is being performed. Another γ-ray flare—the second largest observed to date—was detected with *Fermi*/LAT in 2013 March (Mayer et al. 2013). This triggered further observations with Keck, with the *HST*, and with the *Chandra X-ray Observatory*. Here we concentrate on what was learned about the inner knot as a consequence of this campaign. We note that very-high-energy ($E \geqslant 100$ GeV) contemporaneous data from the HESS (H.E.S.S. Collaboration et al. 2014) and VERITAS (Aliu et al. 2014) Cherenkov-telescope arrays found no significant correlation of TeV flux with the flare observed with *Fermi*/LAT.

The observations are presented in Section 2. The measured properties of the knot are given in Section 3. Section 4 compares observations of the inner knot at the different wavelengths. A comparison and an examination of possible correlations of the knot's properties with γ rays detected using the *Fermi*/LAT are discussed in Section 5. Section 6 discusses theoretical implications. Section 7 summarizes our findings.

2. THE OBSERVATIONS

The feature we refer to as the "inner knot" (aka "knot 1," or "synchrotron knot") was discovered by Hester et al. (1995) in a detailed study of the Crab using high-resolution images taken with *HST*. The feature, although resolved in those data, is small ($\approx 0\farcs1$) and close to the pulsar ($\approx 0\farcs6$). The feature was first suggested to be associated with a shock or instability in the jet $\approx$1500 AU from the pulsar, due to its good alignment with the jet and elongation perpendicular to the jet. Later Komissarov & Lyubarsky (2003) proposed, based on two-dimensional (2D) magnetohydrodynamic (MHD) simulations of the pulsar wind nebula, that the knot represents Doppler-boosted emission from an oblique termination shock. Synthetic synchrotron images from these 2D simulations (Komissarov & Lyutikov 2011), and more recently three-dimensional (3D) simulations (Porth et al. 2014), indeed show a knot-like feature when the system is viewed from the proper (and reasonable) orientation. Moreover, the observed high degree of polarization and a position angle aligned with the symmetry axis (Moran et al. 2013) seems to lend further support to the oblique shock scenario.

The salient features of the inner knot deduced prior to our observations indicate that it has a power-law spectrum $F_\nu \propto \nu^{-\alpha}$ with index $\alpha \sim 0.8$ in the IR to optical (Sollerman 2003; Melatos et al. 2005) and, as most recently measured by Moran et al. (2013), the flux varies, the position appears to change, the degree of polarization is very large but does not appear to change with the flux (but see the discussion at the end of Section 5), and the magnetic field (determined from the position angle of the optical polarization) is orthogonal to the axis of symmetry (presumably the spin axis) and consistent with the direction of the field for the rest of the inner nebula.

2.1. Keck

We obtained K'- and H-band near-infrared (NIR) images of the inner 40″ of the Crab Nebula using the Keck Near-infrared Camera 2 (NIRC2; K. Matthews, PI), with laser guide star adaptive optics (AO; Wizinowich et al. 2006). From 2012 February to 2014 January, we obtained 11 observations of the nebula during γ-ray quiescent periods and 1 target-of-opportunity observation (K8) triggered by γ-ray flares. Table 1 summarizes the Keck observations.

Table 1
Summary of the 12 Keck Observations

#	Date	MJD[a]	Instrument[b]	Exposure (s)
K1	2012 Feb 08	55965.285	NIRC2-wide	420
K2	2012 Mar 05	55991.319	NIRC2-wide	420
K3	2012 Dec 22	56283.408	NIRC2-wide	1250
K4	2012 Dec 23	56284.410	NIRC2-narrow	870
K5	2012 Dec 24	56285.388	NIRC2-narrow	1350
K6	2012 Dec 25	56286.390	NIRC2-wide	1125
K7	2013 Feb 06	56329.308	NIRC2-narrow	2020
K8	2013 Oct 22	56587.448	NIRC2-narrow	640
K9	2014 Jan 09	56666.274	NIRC2-wide	1560
K10	2014 Jan 09	56666.377	NIRC2-narrow	2580
K11	2014 Jan 17	56674.325	NIRC2-wide	2270
K12	2014 Jan 17	56674.394	NIRC2-narrow	1260

Notes.
[a] Quoted MJD is at the midpoint of the observation.
[b] Plate scale is $0\farcs04$/pixel for NIRC2-wide; $0\farcs01$/pixel for NIRC2-narrow.

Data reduction was carried out using the pipeline developed by Ghez et al. (2008). Individual frames were sky-subtracted, flat-fielded, bad-pixel-corrected, and corrected for the NIRC2's camera distortion. We used the solution developed by Yelda et al. (2010), which matched the positions of stars in the globular cluster M92 measured with *HST* to those measured in the NIRC2. Frames were checked to ensure that they showed no irregularities in the point-spread function (PSF), and that the Strehl ratio was at least $\sim$0.10. Individual frames were then combined using the Drizzle algorithm (Fruchter & Hook 2002) to provide sub-pixel accuracy and high signal-to-noise images for analysis and modeling (Section 3.1 and Appendix).

The observations were conducted with two different pixel scales, using the NIRC2 "wide" camera, with $0\farcs04$ pixels and a $40'' \times 40''$ field of view, and the NIRC2 "narrow" camera, with $0\farcs01$ pixels and a $10'' \times 10''$ field of view. The total effective exposure times ranged from 420 to $\approx$2600 s. The shorter exposures result in optimal use of 1-hr Target-of-opportunity interrupts—including acquisition, calibration, and sky measurements.

The spatial resolution of Keck's NIRC2 with AO proved to be very effective for resolving the detailed structure and position of the knot. Figure 1 shows the 12 NIRC2 images. In the narrow camera, the center of the pulsar and the center of the knot are separated by $\approx$60 pixels. Typical values for the signal-to-noise ratio of the knot are 5. The PSF of NIRC2 with AO varies slightly in time due to the variable performance of the AO system. As the pulsar and knot are well-resolved from each other in the Keck images, we chose not to deconvolve the PSF from the Keck images.

2.2. HST

Since 2012 January, we have obtained 22 observations using the *HST* Advanced Camera for Surveys (ACS) Wide-field Channel (WFC), with $0\farcs05$ pixels. Each observation comprises four exposures totaling 2000 s and uses a standard 4-point

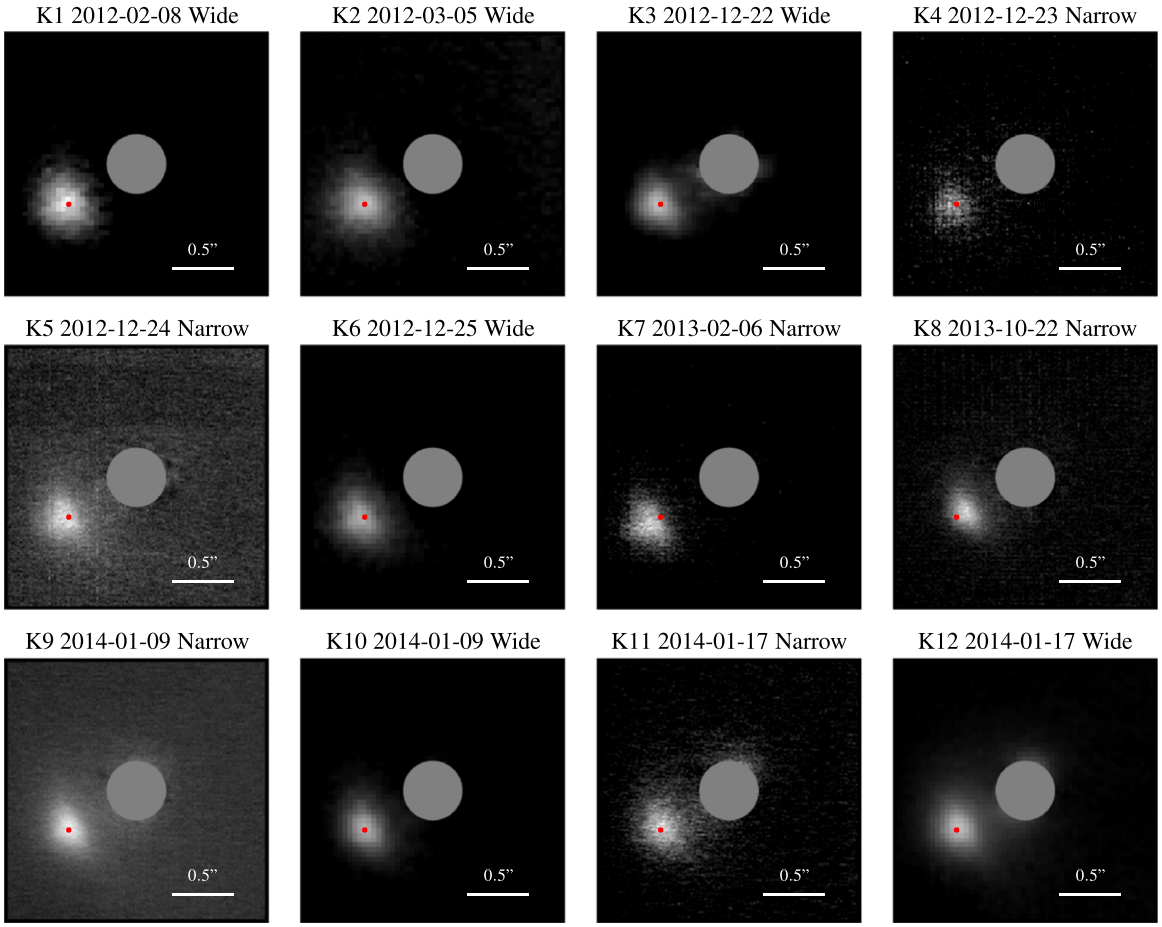

Figure 1. Individual images of the inner knot, with the pulsar removed, from Keck NIRC2 with laser guide star adaptive optics (AO). In each image, the PSF of the pulsar has been subtracted using the scaled PSF of a nearby star and replaced with a gray circle at the original location of the pulsar. Each image is 2.″2 by 2.″2. The images are from the NIRC2-wide camera (0.″04 pixels) or the NIRC2-narrow camera (0.″01 pixels). All images were taken using the K' filter. For positional reference, the red dot marks the average position of the inner knot across all 12 observations.

BOX dithering pattern to fill the inter-chip gap as well as to allow efficient cosmic ray cleaning. We employed the *F*550*M* filter, which is well-suited to sampling continuum emission from the Crab with almost no contamination from line emission.

Table 2 summarizes the observations, listing the date and the mean observing time. The Appendix discusses in detail our analyses of the 22 *HST*/ACS images. Figure 2 displays the processed images, in which we have removed the effects of the *HST*/ACS WFC PSF using singular-value decomposition (SVD) and Richardson–Lucy deconvolution.

2.3. Chandra

Our approach for searching for X-ray emission from the inner knot with *Chandra* involved a special use of both the high time resolution and high spatial resolution of the High-resolution Camera for Spectroscopy (HRC-S) array in timing mode. This approach combines the best spatial resolution and the best time resolution afforded by the *Chandra* instrumentation. To achieve the time resolution, it is vital that the counting rate be below the rate where telemetry is saturated (see, e.g., Tennant et al. 2001). Consequently, the Low-energy Transmission Grating was inserted into the optical path to reduce the flux. As inserting the grating is of itself insufficient to avoid telemetry saturation, the trigger threshold of the HRC-S was raised to reduce the rate of detected events. This approach was first successfully used in a trial experiment (ObsID 11245) on 2010 November 16.

The next set of observations in this mode was initiated by us on 2013 March 5 as part of a sequence triggered by a γ-ray flare (Ojha et al. 2013). Unfortunately, the gain of the HRC had dropped since 2010. Consequently, the trigger threshold was too high during our first observation on March 5–6, reducing the counting rate from the pulsar to about a quarter of that expected, dramatically decreasing the number of detected counts. The next HRC observation was to take place on March 10 and the observation had already been fully planned with the commands to execute on board the spacecraft. To replan at this stage would require an extremely short turnaround, yet it was accomplished. Finally, beginning on 2013 October 22, we triggered another sequence of HRC observations in response to the announcement of another γ-ray flare (Buson et al. 2013).

We also consider ObsID 9765, taken on 2008 January 22. For this observation the HRC was operated in a more standard configuration with the threshold set at the nominal value. However, to reduce the count rate, a blade was inserted into the optical path, which is no longer allowed. This blade also reduced the diffracted flux in one direction. By chance, this reduction is greatest near the nominal location of the knot. This reduction, together with a long integration time for this observation, results in ObsID 9765 providing the best data

Table 2
Summary of the 22 *HST* Observations

#	Date	MJD[a,b]
H1	2012 Jan 08	55934.797
H2	2012 Feb 10	55967.170
H3	2012 Mar 12	55998.414
H4	2012 Apr 22	56039.850
H5	2012 Aug 16	56155.336
H6	2012 Sep 10	56180.960
H7	2013 Jan 10	56302.992
H8	2013 Feb 24	56347.055
H9	2013 Mar 06	56357.023
H10	2013 Apr 01	56383.320
H11	2013 Apr 14	56396.113
H12	2013 Aug 13	56517.710
H13	2013 Oct 20	56585.793
H14	2013 Oct 29	56594.700
H15	2013 Dec 01	56627.273
H16	2014 Jan 20	56677.530
H17	2014 Apr 13	56760.900
H18	2014 Aug 10	56879.375
H19	2014 Aug 21	56890.094
H20	2014 Nov 16	56977.820
H21	2015 Jan 21	57043.620
H22	2015 Apr 16	57128.670

Notes.
[a] Quoted MJD is at the midpoint of the observation.
[b] Plate scale is $0\farcs05$/pixels.

for study of the knot. Table 3 summarizes the relevant *Chandra* observations.

3. PROPERTIES OF THE KNOT

Each Keck (Figure 1) or *HST* (Figure 2) image obtained in this campaign clearly shows the inner knot at nominally $0\farcs65$ southeast of the pulsar. As already noted in previous *HST* observations (Hester et al. 1995; Hester 2008; Moran et al. 2013), this feature is persistent but not static.

Here we report on our analysis of the Keck (Section 3.1) and *HST* (Section 3.2) images to measure the properties of the inner knot, changes with time, and correlations of intrinsic properties with the pulsar–knot separation. Figure 3 defines the lowest-order geometric properties of the knot: r_0, the projected separation of the knot's center from the pulsar; ψ_0, the position angle (east of north) on the sky from the pulsar to the knot's center; FWHM$_r$ and FWHM$_t$, the full widths at half maximum of the knot in the radial and tangential directions, respectively.

3.1. Keck

Table 4 lists the best-fit values of the model parameters for the inner knot for each of the 12 Keck observations based upon the analysis and modeling described in the Appendix. Besides listing the geometric properties (r_0, ψ_0, FWHM$_r$, and FWHM$_t$), the table lists F_k/F_p, the ratio of the flux in the knot to that in the pulsar. We tabulate the flux ratio rather than an absolute flux because the measured fluxes of five stars in the NIRC2-wide camera's field differed from one observation to the next. This occurs because the nebular background varies spatially across the detector in a non-trivial way, making it difficult to precisely determine the flux of any given source. Figure 4 plots ψ_0, FWHM$_r$, and FWHM$_t$, and F_k/F_p against r_0 for the Keck data.

We test for a possible correlation of each property p with separation r_0 from the pulsar, of the form $p(r_0) = p(r_1)[r_0/r_1]^q$, where reference separation r_1 is the geometric average of the 12 Keck measurements. We fit the position angle of the knot, ψ_0, to the linear regression $\psi_0 = \psi_0(\langle r_0\rangle) + \psi_0'(\langle r_0\rangle)[r_0 - \langle r_0\rangle]$, where $\langle r_0\rangle$ is the arithmetic average. Table 5 tabulates the results of the regression analyses of the inner knot's intrinsic properties with its (projected) separation from the pulsar. Based upon the F-test probability, the power-law regression analysis finds marginally significant correlations of the radial width, tangential width, and peak intensity (surface brightness) with separation. The correlations to the separation of the knot's flux and position angle are not significant.

3.2. HST

Table 6 lists the best-fit values of the model parameters for the inner knot for each of the 22 *HST* observations based upon the modeling and analysis described in the Appendix. Besides listing the geometric properties (r_0, ψ_0, FWHM$_r$, and FWHM$_t$), the table lists F_k/F_p, the ratio of the flux in the knot to that in the pulsar, and S_k/F_p, the peak surface brightness scaled to the pulsar flux. Although we expected the pulsar flux to be steady, we measured small ($2.5-\sigma$) variations and thus decided to work with the flux ratio F_k/F_p.

In the Appendix we discuss two ways of analyzing the *HST* data. Table 6 presents the results for one of these methods. However, our general conclusions concerning the knot's optical properties are for the most part the same for either analysis. Figure 5 plots the knot properties versus the pulsar–knot separation, based upon the *HST* data.

As with the Keck data, we perform a regression analysis of each property p with separation r_0. (Table 7). Similarly, r_1 is the geometric average of the 22 *HST* observations; $\langle r_0\rangle$, the arithmetic average.

Based upon the F-test probability, the power-law regression analysis finds statistically significant correlations of the tangential width FWHM$_t$ with separation r_0 from the pulsar, as well as the previously known (Moran et al. 2013) anti-correlations of flux F_k and of peak surface brightness S_k with separation. The correlations of radial width FWHM$_r$ and of position angle ψ_0 with separation r_0 are less strong. We note that we find similar correlations—except for the flux—using the more traditional *HST* analysis methods described in the Appendix.

3.3. Chandra

For the *Chandra* data, the main question is whether X-ray emission from the knot can be detected—especially in the vicinity of the bright, X-ray-emitting pulsar. The answer, unfortunately, is "No" and here we set an informative upper limit to the X-ray flux of the inner knot relative to that of the pulsar.

Table 8 shows the number of counts in each of three extraction regions: (1) centered on the approximate location of the optical knot, (2) centered on the pulsar, and (3) placed on a reference region to estimate the background. Details may be found in the Appendix and are illustrated in Figure 6. The analysis was performed both for the full phase-averaged data and for the data at pulse minimum. Consider, for example, the

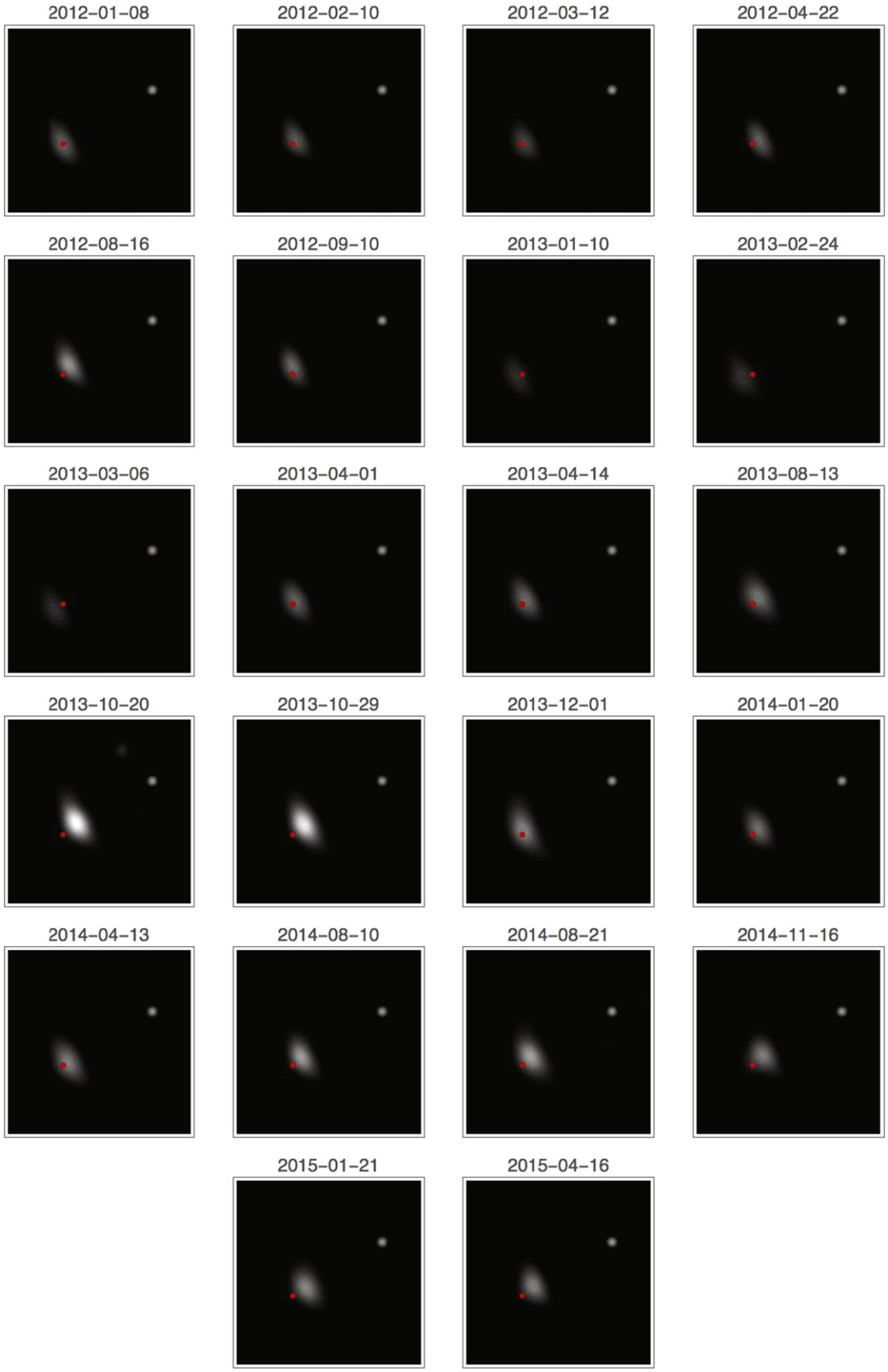

Figure 2. *HST*-SVD-processed images of the Crab pulsar and inner knot after removing the effects of the *HST*/ACS WFC point-spread function. For positional reference, the red dot in each image marks the position of the inner knot during the first of these 22 observations. The *HST* observations of 2013 March 06 (H9) and of 2013 October 29 (H14) each occurred at the peak of a γ-ray flare (Figure 8).

Table 3
Summary of the *Chandra* Observations

#	ObsID	Date	MJD[a]	Exposure (s)
C1	09765	2008 Jan 22	54487.670	95082
C2	11245	2010 Nov 16	55516.294	22039
C3	14684	2013 Mar 05	56356.972	19485
C4	14686	2013 Mar 10	56361.338	20052
C5	14687	2013 Mar 17	56368.324	16718
C6	16244	2013 Oct 19	56584.658	20048
C7	16246	2013 Oct 22	56587.515	20013
C8	16247	2013 Oct 24	56589.007	19770

Note.
[a] Quoted MJD is at the start of the observation.

phase-averaged data for ObsID 11245. Comparing the inner knot counts to the background (Table 8) we find an excess of 167 counts. If the excess were really due to the knot, we would accordingly expect an excess of 50 (=167 × 0.3) counts at phase minimum. As this was not the case, we attribute the excess to the wings of the PSF from the pulsar and posit that it is due to the spring/fall asymmetry discussed in the Appendix. As the impact of that asymmetry is below the statistical noise for the data taken at phase minimum, we then use the phase minimum data to derive upper limits. We convert our phase minimum upper limit into a phase-averaged upper limit by accounting for the 0.3 phase duration of the minimum and then divide by the phase average pulsar flux. The results are listed in the last column in Table 8.

4. COMPARISON AMONG OBSERVATIONS OF THE INNER KNOT

Our *Chandra* observations were unable to detect X-ray flux from the knot, setting a 3σ upper limit to the ratio of knot flux to pulsar flux $F_k/F_p < 0.0022$. This upper limit is 20–40 times smaller than the ratio measured in the optical ($F_k/F_p = 0.044 \pm 0.001$) and in the near-IR ($F_k/F_p = 0.063 \pm 0.003$), indicating that the optical–X-ray spectral index of the knot is significantly steeper (by at least 0.5) than that of the pulsar.

Both our infrared and optical observations detected time variability in the pulsar–knot separation, with roughly consistent separations when measured contemporaneously (see the lower portion of Figure 7). Correlations of knot properties with pulsar–knot separation are very strong for the optical measurements but rather weak for the infrared measurements. We attribute this difference to a combination of factors—including poorer statistics for the much shorter NIR measurements and a number of systematic effects, resulting in part from the NIR PSF and background varying across the field and in time. As the lower portion of Figure 7 and Table 4 indicate, NIR-measured separations at essentially the same epoch exhibit a scatter that is substantially larger than the quoted statistical errors in the measurement, thus suggesting the presence of unaccounted systematic errors.

5. COMPARISON WITH γ-RAY FLUXES

It is clear from the previous sections that the intrinsic properties of the optical knot are correlated with its projected separation from the pulsar. The correlation for the NIR knot is but marginally significant. Thus, in searching for any relationship between the knot and the γ-ray flux, we concentrate on the pulsar–knot separation versus the γ-ray flux. The analysis performed to reduce the *Fermi*/LAT data is the same as that described in Mayer et al. (2013).

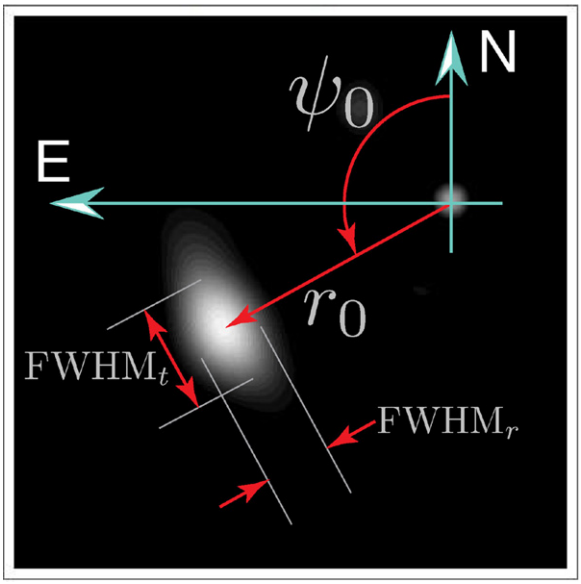

Figure 3. Geometric properties of the inner knot: r_0, the projected separation of the knot from the pulsar; ψ_0, the position angle (east of north) on the sky of the pulsar–knot separation; FWHM$_r$, the full width at half maximum of the knot in the radial direction; and FWHM$_t$, the FWHM of the knot in the tangential direction. The underlying image is from the 2013 October 20 *HST* observation (H13), which exhibits the minimum separation and maximum optical flux observed during this campaign.

Table 9 lists the dates and separations measured in the Keck and in the *HST* observations, followed by the corresponding 12-hr-average *Fermi*/LAT $\geqslant 100$ MeV fluxes. The upper portion of Figure 7 shows the *Fermi*/LAT flux as a function of time covering the interval when our Keck and *HST* observations were made. The vertical lines identify times when observations were made with Keck (red) or with *HST* (green). The lower portion of Figure 7 plots the pulsar–knot separations on the same timescale. Figure 8 expands Figure 7 at the times of the three largest γ-ray flaring episodes during our observational campaign. Note that the *HST* observations of 2013 March 06 (H9) and of 2013 October 29 (H14) each fortuitously occurred within the peak of a γ-ray flare.

Interestingly, a comparison of the γ-ray light curve with the time series of pulsar–knot separations (Figure 7) finds that the most energetic γ-ray flare (2013 March) during the observational campaign occurred near the time of the greatest pulsar–knot separation. Curiously, however, this comparison also finds that the second most energetic flaring episode (2013 October) occurred near the time of the least pulsar–knot separation. The third most energetic flaring episode (2014 August) took place while the separation was midway between the average and minimum measured during the campaign. The inner knot's excursion near the 2013 March γ-ray flare and its incursion near the 2013 October flare were transient, with timescales of a few weeks—significantly longer than the time scale of a few days (or less) of a γ-ray flare. The lesser incursion of the knot near the 2014 August flaring episode was even slower.

As the timescales for motion of the inner knot appear to be an order of magnitude longer than those for the γ-ray flaring, there can be no simple correlation of γ-ray flux with pulsar–

Table 4
Knot Properties Based upon Analysis of the Keck Data

#	r_0 ″	ψ_0 °	FWHM$_r$ ″	FWHM$_t$ ″	F_k / F_p
K1	0.6711 ± 0.0015	118.50 ± 0.16	0.3931 ± 0.0040	0.4719 ± 0.0051	0.0639 ± 0.0045
K2	0.6577 ± 0.0015	121.00 ± 0.13	0.4121 ± 0.0035	0.4252 ± 0.0042	0.0626 ± 0.0067
K3	0.6893 ± 0.0011	122.64 ± 0.11	0.3215 ± 0.0028	0.3948 ± 0.0039	0.0804 ± 0.0074
K4	0.7118 ± 0.0021	120.96 ± 0.18	0.3401 ± 0.0051	0.4081 ± 0.0059	0.0473 ± 0.0003
K5	0.6981 ± 0.0007	121.20 ± 0.07	0.2983 ± 0.0019	0.3767 ± 0.0024	0.0555 ± 0.0005
K6	0.7164 ± 0.0010	120.79 ± 0.12	0.3375 ± 0.0029	0.4238 ± 0.0042	0.0599 ± 0.0085
K7	0.7756 ± 0.0013	121.93 ± 0.12	0.3355 ± 0.0034	0.4049 ± 0.0038	0.0662 ± 0.0004
K8	0.5722 ± 0.0004	120.33 ± 0.06	0.2216 ± 0.0011	0.3172 ± 0.0015	0.0621 ± 0.0005
K9	0.6543 ± 0.0006	121.46 ± 0.08	0.2958 ± 0.0018	0.4030 ± 0.0024	0.0708 ± 0.0047
K10	0.6257 ± 0.0003	115.77 ± 0.03	0.2689 ± 0.0007	0.3683 ± 0.0009	0.0663 ± 0.0006
K11	0.6371 ± 0.0008	121.49 ± 0.10	0.3119 ± 0.0022	0.3787 ± 0.0029	0.0647 ± 0.0078
K12	0.6438 ± 0.0009	118.99 ± 0.09	0.3248 ± 0.0023	0.3766 ± 0.0025	0.0574 ± 0.0001

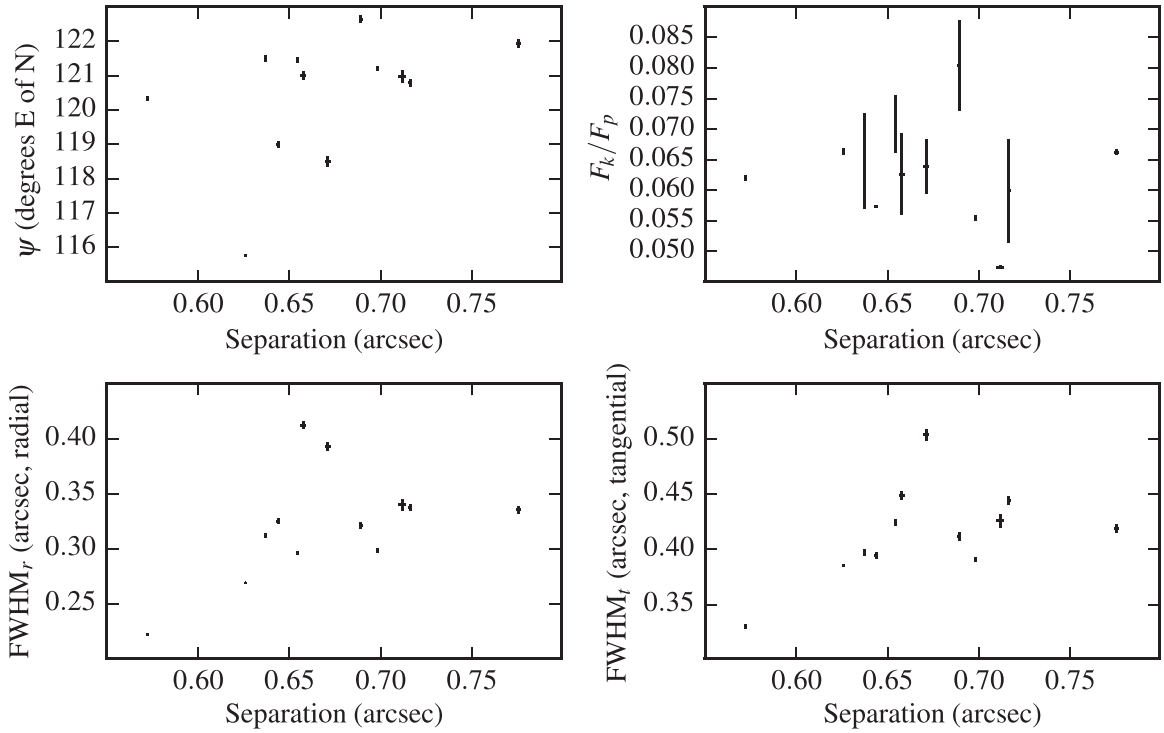

Figure 4. Variation of the Keck-measured knot properties vs. separation of the inner knot from the pulsar.

Table 5
Results of Regression Analyses for the 12 Keck Observations

Power-law for $r_1 = 0.''6692$ Property	Unit	$p(r_1)$	Power-law Index q	Probability
FWHM$_r$	″	0.3180 ± 0.0132	1.19 ± 0.54	5.4E-2
FWHM$_t$	″	0.3941 ± 0.0093	0.75 ± 0.31	3.8E-2
S_k	$F_p/(″)^2$	0.439 ± 0.033	−2.14 ± 0.97	5.2E-2
F_k	F_p	0.0626 ± 0.0025	−0.20 ± 0.53	7.1E-1
Linear for $\langle r_0 \rangle = 0.''6711$ Property		$\psi_0(\langle r_0 \rangle)$	$d\psi_0/dr_0$	
ψ_0	°, °/″	120.42 ± 0.51	15.2 ± 10.2	1.7E-1

Table 6
Knot Properties Based upon SVD Analysis of the 22 *HST* Observations (See the Appendix)

#	r_0 ″	ψ_0 °	FWHM$_r$ ″	FWHM$_t$ ″	S_k e/s/(″)^2	F_k e/s	F_p e/s	F_k F_p
H1	0.6819 ± 0.0023	120.54 ± 0.40	0.1526 ± 0.0056	0.3221 ± 0.0116	1064 ± 33	59.8 ± 3.6	1425 ± 82	0.0420 ± 0.0035
H2	0.6535 ± 0.0024	119.45 ± 0.41	0.1536 ± 0.0058	0.3071 ± 0.0114	1008 ± 32	53.8 ± 3.4	1433 ± 80	0.0375 ± 0.0032
H3	0.6708 ± 0.0022	120.37 ± 0.33	0.1751 ± 0.0052	0.3121 ± 0.0092	902 ± 23	55.0 ± 2.6	1471 ± 64	0.0374 ± 0.0024
H4	0.6356 ± 0.0024	121.74 ± 0.41	0.1465 ± 0.0056	0.2942 ± 0.0110	1053 ± 34	52.3 ± 3.2	1276 ± 80	0.0410 ± 0.0035
H5	0.6166 ± 0.0020	117.90 ± 0.39	0.1406 ± 0.0048	0.3043 ± 0.0102	1256 ± 36	61.1 ± 3.4	1231 ± 84	0.0497 ± 0.0044
H6	0.6577 ± 0.0024	117.62 ± 0.41	0.1456 ± 0.0058	0.3029 ± 0.0112	1102 ± 36	56.7 ± 3.5	1184 ± 86	0.0479 ± 0.0046
H7	0.7240 ± 0.0035	121.17 ± 0.59	0.1704 ± 0.0084	0.3539 ± 0.0176	675 ± 28	44.7 ± 3.9	1422 ± 77	0.0314 ± 0.0032
H8	0.7516 ± 0.0031	119.91 ± 0.50	0.1751 ± 0.0076	0.3533 ± 0.0158	667 ± 25	44.5 ± 3.4	1421 ± 65	0.0313 ± 0.0028
H9	0.7491 ± 0.0033	120.88 ± 0.52	0.1740 ± 0.0080	0.3362 ± 0.0166	728 ± 29	45.8 ± 3.8	1359 ± 73	0.0337 ± 0.0033
H10	0.6614 ± 0.0019	120.60 ± 0.32	0.1598 ± 0.0046	0.3139 ± 0.0090	1098 ± 27	63.3 ± 3.0	1295 ± 72	0.0489 ± 0.0036
H11	0.6557 ± 0.0021	119.39 ± 0.36	0.1639 ± 0.0050	0.3220 ± 0.0098	1090 ± 28	64.9 ± 3.3	1509 ± 77	0.0430 ± 0.0031
H12	0.6324 ± 0.0023	119.28 ± 0.41	0.1691 ± 0.0056	0.3299 ± 0.0110	1028 ± 29	63.4 ± 3.6	1283 ± 83	0.0494 ± 0.0042
H13	0.5687 ± 0.0019	117.85 ± 0.36	0.1426 ± 0.0046	0.2739 ± 0.0082	1668 ± 44	75.6 ± 3.8	1222 ± 106	0.0618 ± 0.0062
H14	0.5849 ± 0.0022	118.82 ± 0.41	0.1441 ± 0.0052	0.2886 ± 0.0098	1583 ± 48	75.6 ± 4.4	1285 ± 118	0.0589 ± 0.0064
H15	0.6624 ± 0.0026	118.59 ± 0.52	0.1476 ± 0.0061	0.3393 ± 0.0144	1105 ± 40	61.8 ± 4.4	1353 ± 100	0.0457 ± 0.0047
H16	0.6299 ± 0.0026	118.82 ± 0.41	0.1640 ± 0.0064	0.2961 ± 0.0106	1084 ± 35	62.1 ± 3.7	1419 ± 98	0.0438 ± 0.0040
H17	0.6448 ± 0.0024	120.88 ± 0.41	0.1611 ± 0.0059	0.3212 ± 0.0109	1164 ± 35	69.6 ± 4.0	1177 ± 99	0.0591 ± 0.0060
H18	0.6063 ± 0.0022	119.62 ± 0.39	0.1481 ± 0.0053	0.2921 ± 0.0097	1289 ± 38	67.1 ± 3.6	1305 ± 96	0.0514 ± 0.0055
H19	0.6106 ± 0.0023	118.99 ± 0.38	0.1498 ± 0.0055	0.2855 ± 0.0098	1200 ± 36	61.9 ± 3.4	1252 ± 90	0.0494 ± 0.0052
H20	0.6004 ± 0.0029	119.39 ± 0.44	0.1827 ± 0.0070	0.2681 ± 0.0113	1111 ± 38	58.4 ± 4.1	1566 ± 95	0.0373 ± 0.0033
H21	0.5773 ± 0.0028	120.37 ± 0.42	0.1701 ± 0.0067	0.2890 ± 0.0103	1153 ± 37	68.3 ± 4.0	1530 ± 107	0.0446 ± 0.0045
H22	0.5929 ± 0.0022	118.93 ± 0.36	0.1593 ± 0.0052	0.2633 ± 0.0089	1202 ± 34	57.2 ± 3.2	1417 ± 80	0.0404 ± 0.0033

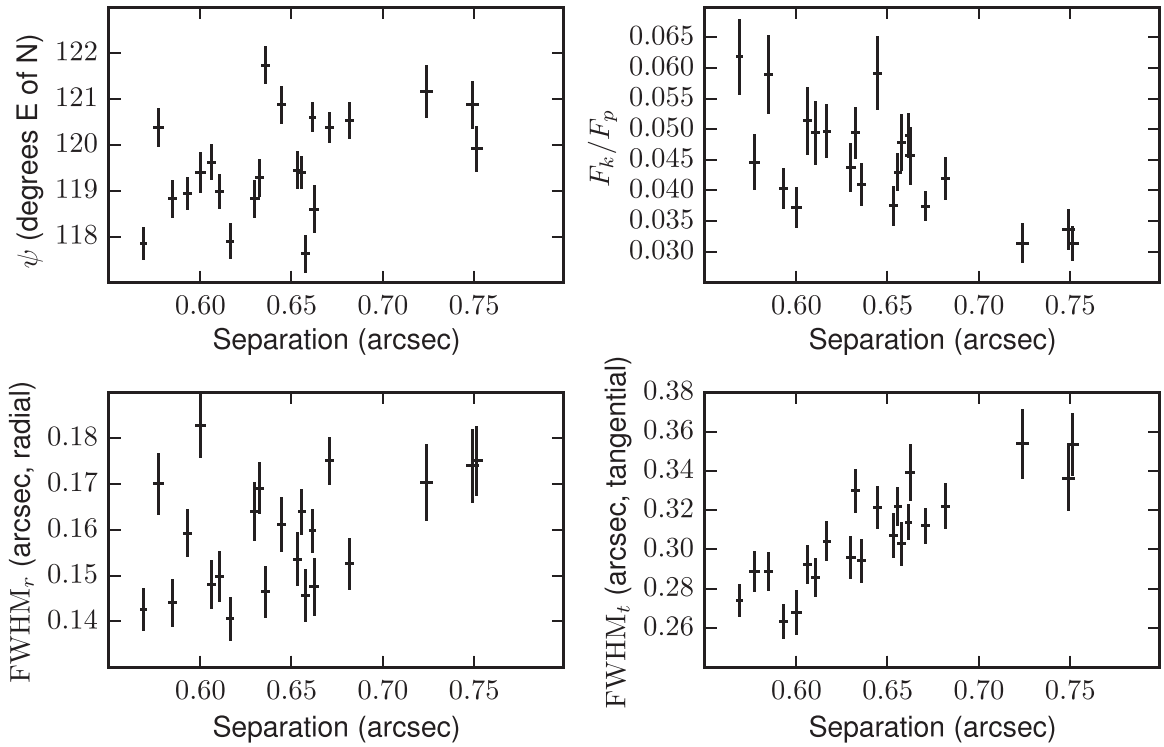

Figure 5. Variation of the *HST*-SVD-measured properties with separation of the inner knot from the pulsar.

knot separation. Indeed, a plot of γ-ray flux measurements that is coincident with the 22 *HST* and 12 Keck observations against the measured pulsar–knot separations (Figure 9) shows no significant correlation. The absence of a simple correlation, the relative sparsity of the near-IR and optical data, and the lack of a detailed physical model make it difficult to relate γ-ray flaring to changes in the pulsar–knot separation. Hence, while this behavior is intriguing, we have not succeeded in deducing a pattern relating the γ-ray flares to the pulsar–knot separation. Of course, it is also possible that no such relationship exists.

We note that Moran et al. (2013) used polarization observations from the *HST* archive to measure a possible change in the linear polarization of the inner knot that occurred a few weeks after an incursion of the inner knot in 2005

Table 7
Results of Regression Analyses for the 22 *HST* Observations Based on the Data in Table 6

Power-law for $r_1 = 0\farcs6421$ Property	Unit	$p(r_1)$	Power-law Index q	Probability
FWHM_r	$''$	0.1584 ± 0.0025	0.41 ± 0.21	5.9E-2
FWHM_t	$''$	0.3067 ± 0.0029	0.92 ± 0.12	2.9E-7
S_k	$F_\mathrm{p}/('')^2$	0.796 ± 0.029	−2.77 ± 0.47	9.8E-6
F_k	F_p	0.0440 ± 0.0014	−1.70 ± 0.40	4.1E-4
Linear for $\langle r_0 \rangle = 0\farcs6440$ Property		$\psi_0(\langle r_0 \rangle)$	$d\psi_0/dr_0$	
ψ_0	°, °/″	119.60 ± 0.22	10.2 ± 4.4	3.2E-2

Table 8
Results of the *Chandra* Analysis

ObsID	Pulse Average			Pulse Minimum			$F_\mathrm{k}/F_\mathrm{p}$
	Pulsar	Knot	Background	Pulsar	Knot	Background	3σ
09765	51844	2963	3704	845	57	72	<0.0022
11245	5630	1018	851	88	16	12	<0.0094
Last 6	13549	2622	2503	203	39	44	<0.0067

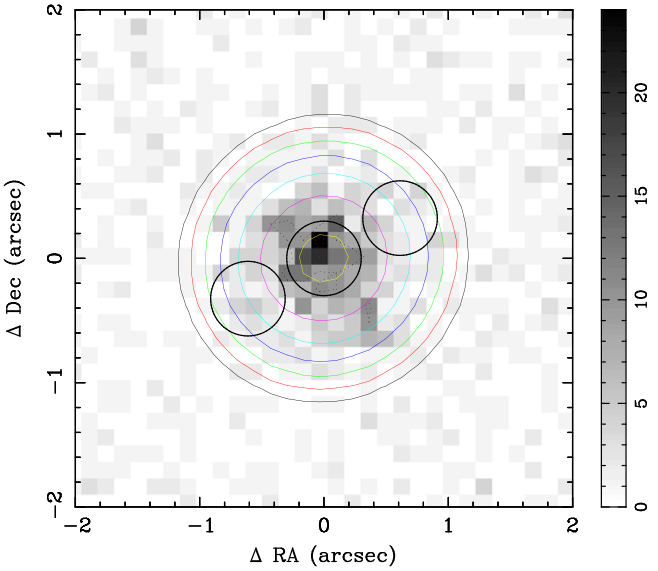

Figure 6. *Chandra* image at pulse minimum from the sum of the last six flaring data sets in Table 3. The three small black circles show $0\farcs3$-radius extraction regions, the central of which is used to estimate the pulsar flux. The circle, at a position angle $\psi = 120°$ east of north and $0\farcs65$ from the pulsar, is roughly centered on the average optical location of the knot. Data in the opposite small circle (the one to the NW where N is up) are used to estimate background. Large circles show the best-fit Gaussian to the phase-average pulsar data at intensity levels of 10, 20, 40, 80, 160, 320, and 640 cts/pixel illustrating the level of impact of the PSF at the site of the knot—i.e., slight but non-negligible. The intensity level is shown by the grayscale bar on the right.

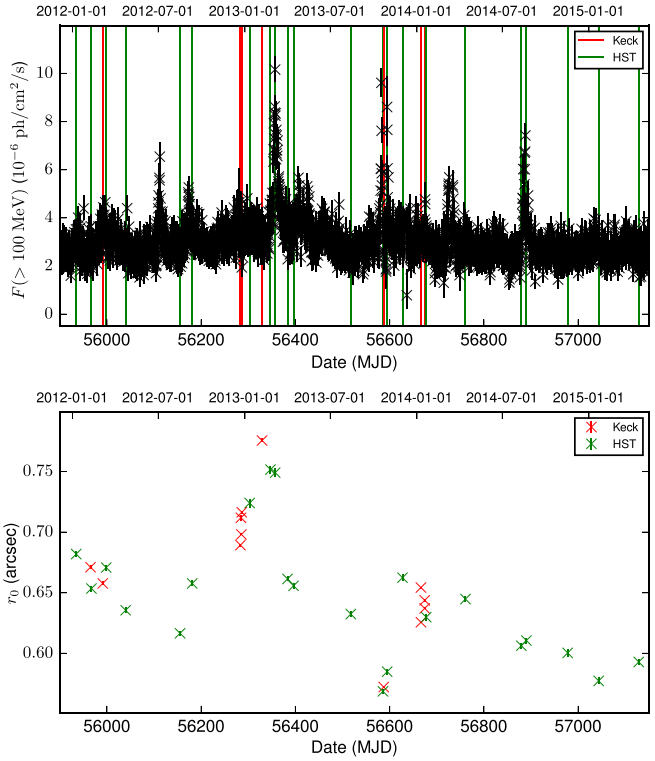

Figure 7. *Fermi*/LAT 12 hr average flux (upper panel) and pulsar–knot separation (lower panel) vs. time, for Keck (red) and *HST* (green) observations.

November, with an amplitude and timescale comparable to those of the 2013 October incursion that we observed. Like the 2013 October incursion, the 2005 November incursion coincided with an increase in the inner knot's optical flux. While the significance of the polarization change was marginal based upon the authors' conservative statistical analysis, we conclude that optical polarization measurements may be useful for seeking a relationship between γ-ray flaring and inner knot behavior.

6. IMPLICATIONS FOR THEORETICAL MODELS

In the basic model of the Crab Nebula (e.g., Rees & Gunn 1974), the pulsar wind passes through a shock at a radius $\sim 3 \times 10^{17}$ cm where the wind momentum flux balances the nebular pressure. However, the wind should be anisotropic. For example, the momentum flux in a split-monopole $\propto \sin^2\theta$ (Bogovalov 1999) and recent simulations suggest $\propto \sin^4\theta$ (Tchekhovskoy et al. 2013, 2015) where θ is the polar angle.

Table 9
Fermi/LAT 12 hr-average Fluxes and Pulsar–Knot Separations as Measured with Keck and *HST* (SVD Analysis)

#	Date	$t_{\rm mid}$ MJD	r_0 $''$	*Fermi*/LAT $\geqslant$100 MeV 10^{-6} ph s^{-1} cm^{-2}
H1	2012 Jan 08	55934.797	0.6819 ± 0.0023	2.74 (+0.42, −0.39)
K1	2012 Feb 08	55965.280	0.6711 ± 0.0015	2.64 (+0.44, −0.40)
H2	2012 Feb 10	55967.171	0.6535 ± 0.0024	2.02 (+0.43, −0.39)
K2	2012 Mar 05	55991.311	0.6577 ± 0.0015	2.70 (+0.38, −0.36)
H3	2012 Mar 12	55998.414	0.6708 ± 0.0022	3.70 (+0.43, −0.40)
H4	2012 Apr 22	56039.850	0.6356 ± 0.0024	2.40 (+0.50, −0.46)
H5	2012 Aug 16	56155.336	0.6166 ± 0.0020	2.87 (+0.44, −0.44)
H6	2012 Sep 10	56180.960	0.6577 ± 0.0024	3.06 (+0.37, −0.37)
K3	2012 Dec 22	56283.381	0.6893 ± 0.0011	2.64 (+0.45, −0.45)
K4	2012 Dec 23	56284.403	0.7118 ± 0.0021	4.56 (+0.53, −0.50)
K5	2012 Dec 24	56285.379	0.6981 ± 0.0007	3.59 (+0.50, −0.45)
K6	2012 Dec 25	56286.370	0.7164 ± 0.0010	1.89 (+0.43, −0.39)
H7	2013 Jan 10	56302.992	0.7240 ± 0.0035	2.68 (+0.51, −0.51)
K7	2013 Feb 06	56329.248	0.7756 ± 0.0013	3.17 (+0.50, −0.50)
H8	2013 Feb 24	56347.055	0.7516 ± 0.0031	4.29 (+0.55, −0.51)
H9	2013 Mar 06	56357.023	0.7491 ± 0.0033	10.88 (+0.47, −0.47)
H10	2013 Apr 01	56383.320	0.6614 ± 0.0019	4.05 (+0.50, −0.50)
H11	2013 Apr 14	56396.113	0.6557 ± 0.0021	3.43 (+0.50, −0.50)
H12	2013 Aug 13	56517.710	0.6324 ± 0.0023	2.56 (+0.38, −0.35)
H13	2013 Oct 20	56585.793	0.5687 ± 0.0019	3.83 (+0.23, −0.23)
K8	2013 Oct 22	56587.443	0.5722 ± 0.0004	0.70 (+1.41, −0.51)
H14	2013 Oct 29	56594.700	0.5849 ± 0.0022	7.08 (+0.79, −0.79)
H15	2013 Dec 01	56627.273	0.6624 ± 0.0026	2.76 (+0.47, −0.45)
K9	2014 Jan 09	56666.316	0.6543 ± 0.0006	3.14 (+0.40, −0.40)
K10	2014 Jan 09	56666.438	0.6257 ± 0.0003	3.13 (+0.39, −0.37)
K11	2014 Jan 17	56674.356	0.6371 ± 0.0008	4.29 (+0.46,−0.45)
K12	2014 Jan 17	56674.400	0.6438 ± 0.0009	3.93 (+0.39, −0.37)
H16	2014 Jan 20	56677.530	0.6299 ± 0.0026	3.37 (+0.37, −0.37)
H17	2014 Apr 13	56760.900	0.6448 ± 0.0024	3.84 (+0.52, −0.52)
H18	2014 Aug 10	56879.375	0.6063 ± 0.0022	2.50 (+0.41, −0.41)
H19	2014 Aug 21	56890.094	0.6106 ± 0.0023	3.56 (+0.26, −0.25)
H20	2014 Nov 16	56977.820	0.6004 ± 0.0029	2.50 (+0.43, −0.39)
H21	2015 Jan 21	57043.620	0.5773 ± 0.0028	3.05 (+0.36, −0.34)
H22	2015 Apr 16	57128.670	0.5929 ± 0.0022	2.62 (+0.43, −0.43)

As a result, the shock is likely to be quite oblate. The sections of the shock near the poles would be oblique and much closer to the pulsar than the equatorial part. The observed radiation presumably comes from relativistic particles (electrons or positrons) accelerated behind the shock. Since the outflow from an oblique shock can remain relativistic, we would be able to see a compact, emitting feature (the inner knot) if the relativistic outflow happens to be aligned with our line of sight so that its emission is beamed. The inner knot should appear to us as having some offset from the pulsar due to the deflection of the outflow from its presumed radial motion (Figure 10). If the shock is approximately axisymmetric as one would expect, the projected emitting site would fall on the projected symmetry axis, leading to an alignment with the jet. The shape of the inner knot should also be more or less symmetric about the axis; whether it is elongated parallel or perpendicular to the axis depends on the geometry of the oblique shock. Furthermore, the synchrotron emission should be linearly polarized (Komissarov & Lyutikov 2011; Y. Yuan & R. Blandford 2015, in preparation).

The shock model predicts that the scaling between the observed properties of the knot—projected pulsar–knot separation r_0, tangential angular width FWHM$_t$, radial angular width FWHM$_r$, and surface brightness $S_{\rm k}$—should be determined by the upstream magnetization $\sigma \equiv B_1^2/\mu_0 n_1 \gamma_1^2 mc^2$ (where m is electron mass and B_1, n_1, γ_1 are upstream magnetic field, proper density, bulk Lorentz factor, respectively) plus three more parameters that characterize the shape of the shock near the emitting site: the unprojected pulsar–knot separation $r_{\rm k}$; the incident angle δ_1, defined to be the angle between upstream velocity and the shock surface as shown in Figure 10; and the shock poloidal radius of curvature $R_{\rm c}$.

Let the outflow be deflected from the radial direction by an angle Δ at the shock. We then have $r_0 = r_{\rm k}\Delta$. The knot tangential size is determined by the Doppler beaming and the shock radius of curvature in the toroidal direction as FWHM$_t \approx 2r_{\rm k}/\gamma$, where γ is the downstream Lorentz factor. In the simplest shock model with an isotropic plasma, both Δ and γ are functions of σ and δ_1: $\Delta = \delta_1 - \arctan(\chi \tan \delta_1)$ and $\gamma = 1/(\sin \delta_1 \sqrt{1-\chi^2})$, where $\chi \equiv v_{2\perp}/v_{1\perp} = B_1/B_2 = (1 + 2\sigma + \sqrt{16\sigma^2 + 16\sigma + 1})/6(1+\sigma)$ is the compression ratio at the shock, $v_{1,2\perp}$ being the component of upstream/downstream velocity perpendicular to the shock (Komissarov & Lyutikov 2011). The radial knot size FWHM$_r$ should also be proportional to $r_{\rm k}/\gamma$ but will have an additional factor involving the ratio $R_{\rm c}/r_{\rm k}$.

As to the intensity, we assume that the emitting particles have a power-law distribution $\propto n'\gamma'^{-p}$ in the fluid rest frame, where n' and γ' are particle density and Lorentz factor in the

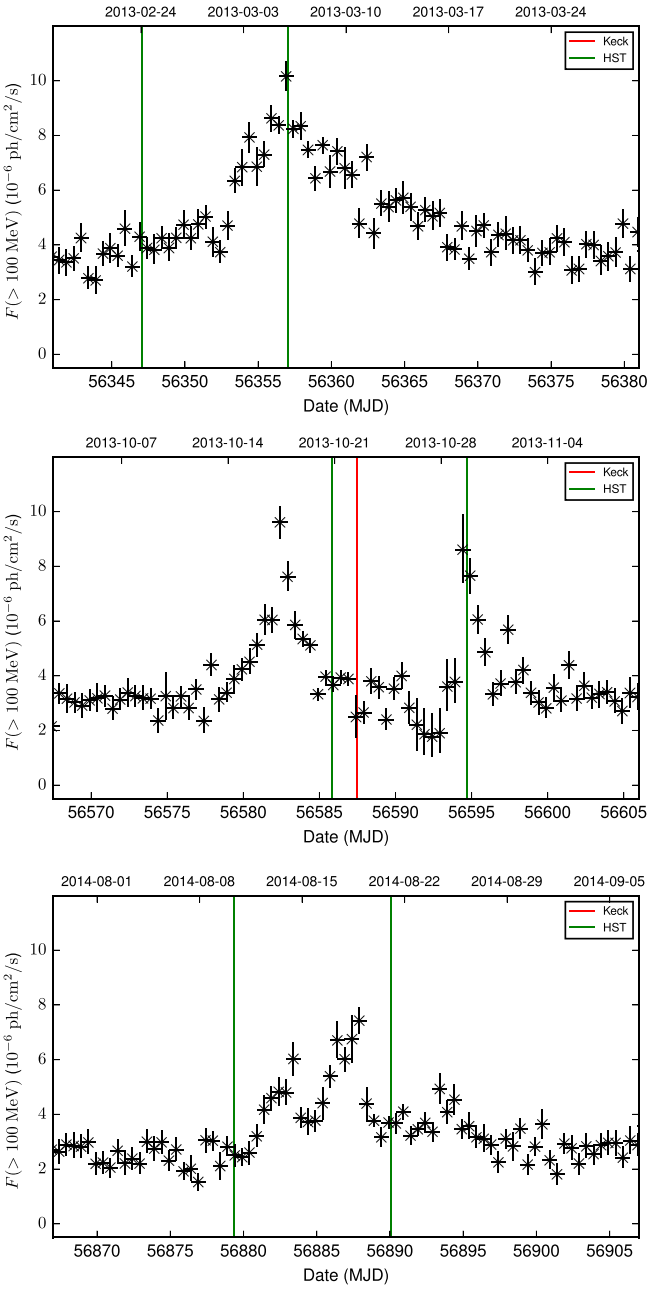

Figure 8. *Fermi*/LAT 12 hr average fluxes during Keck (red) and *HST* (green) observations at the time of the largest γ-ray flares in 2013 March (top), in 2013 October (middle), and in 2014 August (bottom).

same reference frame, and $p \sim 2.6$ from the measured spectral index of the knot (Sollerman 2003; Melatos et al. 2005).

The emissivity in the fluid rest frame is $j'_{\nu'}(\nu') \propto n' B'^{(p+1)/2} \nu'^{-(p-1)/2}$, where B' and ν' are the magnetic field and the radiation frequency measured in this reference frame. After transforming to the nebula frame, the emissivity has a dependence on the flow Lorentz factor γ, particle (improper) number density n, and magnetic field B as follows: $j_\nu \propto \mathcal{D}^{2+(p-1)/2}(n/\gamma)(B/\gamma)^{(p+1)/2}$, where $\mathcal{D} = \nu/\nu' = \sqrt{1-\beta^2}/(1-\boldsymbol{\beta}\cdot\boldsymbol{n})$ is the Doppler factor, in which $\boldsymbol{\beta}$ is the flow velocity and $\boldsymbol{n}$ is a unit vector along the direction of the line of sight. The surface brightness corresponds to the emissivity integrated along the line of sight in the nebular frame: $S_\nu = \int j_\nu dl$. To estimate the peak surface brightness,

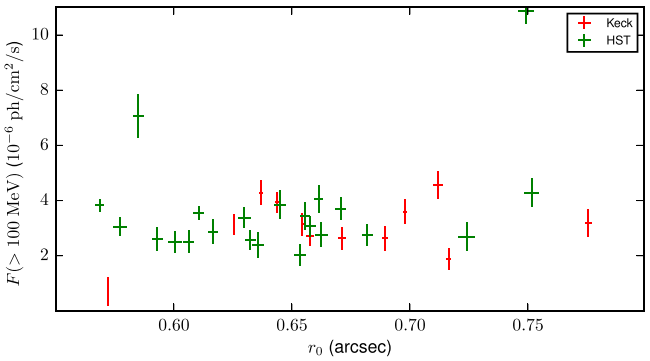

Figure 9. *Fermi*/LAT 12-hr-average fluxes centered on the times of Keck (red) and *HST* (green) measurements of pulsar–knot separations.

one takes the maximum Doppler factor $\mathcal{D} \approx 2\gamma$, and we get $S_{\nu,\mathrm{peak}} \propto nB^{(p+1)/2}\ell$ where ℓ is an estimation of the length of the emitting region along the line of sight. As roughly $B \propto r_\mathrm{k}^{-1}$ and $n \propto r_\mathrm{k}^{-2}$, we have $S_{\nu,\mathrm{peak}} \propto r_\mathrm{k}^{-2-(p+1)/2}\ell$.

These previous relations allow us to set the constraints discussed below using both the steady and variable properties of the knot.

6.1. Variability

In the shock model, variability can arise either upstream or downstream of the shock. First, stress tensor variation in the nebula can cause the shock radius and shape to vary over time. Three-dimensional MHD simulations (Porth et al. 2014) show that even if the upstream condition is fixed, the post-shock flow can be quite variable: there is vortex-shedding from the termination shock, and the shock constantly interacts with waves and vortices in the nebula. Those variations are expected to be mostly magnetic in origin, and the interactions between the shock and the downstream flow are quite nonlinear. The picture is similar to earlier 2D simulations (e.g., Camus et al. 2009) except that the kink instability sets in so that the hoop compression is less prominent as in the 2D case; also short-term variability is less pronounced. The 3D simulations give a typical variation timescale of less than one year.

Now suppose that the change of downstream pressure causes the shock radius r_k to change. For simplicity we first assume that Δ, ℓ, γ, and p stay more or less the same, then from the above scaling relations, we have $S_{\nu,\mathrm{peak}} \propto r_0^{-2-(p+1)/2}$, $\mathrm{FWHM}_t \propto r_0$, and knot flux $F_\nu \propto S_{\nu,\mathrm{peak}}\,\mathrm{FWHM}_t\,\mathrm{FWHM}_r \propto r_0^{-(p+1)/2}$, assuming FWHM_r to also be roughly proportional to r_k. In reality Δ, ℓ, and γ change with the shock radius r_k as well, as the shock shape and upstream incident angle δ_1 vary. Consequently, the observed correlation is more complicated and less clean; however, the general trend is consistent with our expectation of the shock model. In the 3D simulation of Porth et al. (2014), the synthetic images of the knot show a variation consistent with the observations of Moran et al. (2013), suggesting that downstream variation of the shock could provide a good explanation for the knot variability.

Variations initiated by the pulsar can also cause the knot properties to change. In such a scenario, the shortest possible variation timescale is $t_v \sim r_\mathrm{k}(1-\cos(1/\gamma))/c \sim r_\mathrm{k}/(2\gamma^2 c)$ $\sim 1\,\mathrm{day}(r_\mathrm{k}/10^{17}\,\mathrm{cm})(\gamma/5)^{-2}$ up to 10% inaccuracy assuming $\gamma \gtrsim 3$. However, there is no evidence in the pulsar timing that this is actually happening.

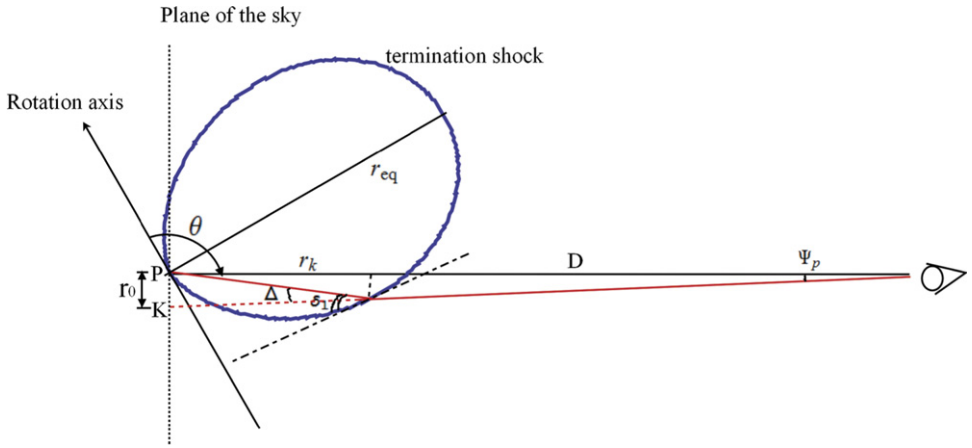

Figure 10. Geometry of the termination shock on the meridional plane determined by the pulsar rotation axis and the observer's line of sight toward the pulsar (point P). The angle between the line of sight and the pulsar rotation axis is $\theta_{ob} = 2\pi/3$, consistent with that measured by Ng & Romani (2008). The inner knot (point K) is projected on the plane of the sky at an angle of $\Psi_p = r_0/D \approx 0\farcs65$ southeast of the pulsar. (NB: Throughout this paper, r_0 appears in units of arcseconds.) The angle between the upstream velocity and the shock surface is δ_1; the outflow is deflected from the radial direction by an angle Δ.

6.2. Time-averaged Properties of the Knot

The properties of the knot may be used to set constraints on the flow composition and how much dissipation occurs at the shock. One constraint comes from geometrical relations among the three measured angles r_0, FWHM$_t$, and FWHM$_r$. For the simplest shock model, we have $r_0 = r_k\Delta$ and FWHM$_t \approx r_k/\gamma$, where Δ and γ only depend on σ and δ_1, such that the ratio FWHM$_t/r_0$ sets limit on σ and δ_1. We find that $\mathrm{FWHM}_t/r_0 = 2/(\gamma\Delta) = 2\sin\delta_1\sqrt{1-\chi^2}/[\delta_1 - \arctan(\chi\tan\delta_1)] \geqslant 2.8$, with the minimum at $\sigma = 0$ and $\delta_1 = 0.39$. In contrast, the observation gives FWHM$_t \sim 0.5r_0$, indicating that some important ingredient is missing in the standard shock model. For example, the upstream flow might have already been bent before arriving at the shock; and/or the anisotropic particle distribution downstream might be important in determining the size of the knot. Although more detailed investigations will be described elsewhere, the above discussion on variability and the following discussion on energetics should be valid for quite general shock models.

The shape of the knot also has some interesting implications. In both the *Hubble* and Keck images, the knot is not just a simple ellipse that only involves quadratic terms of coordinates; it has curvature and appears to be convex away from the pulsar ("smile"), so at least a third moment of the coordinates is needed to describe the shape. A simple intuitive picture is based on the geometry that the shock surface is similar to a torus centered on the pulsar and we look through the hole from the bottom. If emission from the shock outflow roughly follows the local toroidal magnetic field, one would imagine the knot to be convex toward the pulsar ("frown")—contradictory to what we see. In fact, we should not overlook the possibility that the outflow may have significant bending downstream. If the outflow bends toward the equator by an angle $\sim 1/\gamma$ within the emission length, we would see the knot more extended (contracted) on the far (near) side with respect to the pulsar, as additional flow lines enter (originally aligned flow lines leave) the emission cone on the corresponding side.

Another constraint comes from the observed flux of the knot. In the K' band, the typical knot–pulsar flux ratio is $\sim$0.063 (Table 4). If we take the photometry of the pulsar from Sandberg & Sollerman (2009), the pulsar K_s band magnitude is 13.80 $\pm$ 0.01, after dereddening with the best-fit value $E(B-V) = 0.52$ (Sollerman et al. 2000) and the extinction law from Fitzpatrick (1999), this corresponds to a flux of 2.2×10^{-26} erg s^{-1} cm^{-2}Hz^{-1}. So the inner knot flux in K' band should be roughly $F_\nu^{\rm knot} = 1.4\times10^{-27}$ erg s^{-1} cm^{-2} Hz^{-1}. Similarly, optical data (Table 6) on average give a dereddened flux of $F_\nu^{\rm knot} = 1\times10^{-27}$ erg s^{-1} cm^{-2} Hz^{-1}. However, we do not attempt here to get a spectral index using the time-averaged fluxes due to the variability of the knot and the fact that most of the multi-wavelength observations are not simultaneous. Previous measurements by Sollerman (2003) and Melatos et al. (2005) indicate that the spectrum of the knot in IR to optical range is a power law $F_\nu \propto \nu^{-\alpha}$ with $\alpha \sim 0.8$, and Melatos et al. (2005) further measured that this power law extends to NUV (160–320 nm), with a flux in NUV $F_\nu^{\rm knot} = 0.12$ mJy $= 1.2\times10^{-27}$ erg s^{-1} cm^{-2} Hz^{-1}—this is the highest energy at which the knot has been measured. A few more recent measurements show slightly different spectral index ranging from 0.63 (Tziamtzis et al. 2009) to 1.3 (Sandberg & Sollerman 2009), but unfortunately these are based on non-simultaneous data. It would be very interesting to refine the spectral measurement using near simultaneous IR/optical images in the future. In what follows we adopt a fiducial spectral model $F_\nu^{\rm knot} \sim 10^{-27}(\nu/10^{15}\,\mathrm{Hz})^{-0.8}$ erg s^{-1} cm^{-2} Hz^{-1} with the caveat that this could change with better observations.

Using the above spectral model, we find that the knot integrated flux in the IR/optical band ($(0.1-2)\times10^{15}$ Hz) is $F_{\rm O/IR}^{\rm knot} = 2.6\times10^{-12}$ erg s^{-1}cm^{-2}. Thus, the luminosity of the knot per steradian is $L_{\rm O/IR,\Omega} = D^2F_{\rm O/IR}^{\rm knot} = 10^{32}$ erg s^{-1}, where $D \sim 2$ kpc is the distance of the Crab. If we define $\epsilon \equiv L_{\rm O/IR,\Omega}/(\dot{E}/4\pi)$, where $\dot{E} = 5\times10^{38}$ erg s^{-1} is the pulsar spin-down power, ϵ can be used as a measure of the radiative efficiency of the shock along the direction of line of sight in IR to optical range. Here we find $\epsilon = 2.5\times10^{-6}$ and the shock is highly adiabatic.

We can obtain an estimation of the enthalpy fraction of IR/optical-emitting particles in the downstream flow

$$\eta(\gamma') = \frac{8}{3}\frac{\gamma t'_{\rm cool}}{t_{\rm flow}}\frac{\nu L_{\nu,\Omega}}{\dot{E}/(4\pi)} = \frac{8}{3}\frac{\gamma t'_{\rm cool}}{t_{\rm flow}}\frac{\nu L_{\nu,\Omega}}{\dot{E}/(4\pi)}, \qquad (1)$$

where $t_{\rm flow}$ is the flow timescale and $t'_{\rm cool} = 6\pi\epsilon_0 m^3c^3/(e^4B'^2\gamma') \approx 10^2\gamma^2 B_{-3}^{-3/2}\nu_{14}^{-1/2}$ years is the synchrotron cooling time of the particles in the fluid rest frame (we have adopted $B = B_{-3}$ mG and $\nu = \nu_{14}10^{14}$ Hz for the numerical value). Thus the particle injection rate per unit steradian in the corresponding energy band is

$$\dot{N}(\gamma') = \frac{3\eta(\gamma')}{4\gamma' mc^2}\frac{\dot{E}}{4\pi\gamma}. \quad (2)$$

Adopting typical values $\gamma = 5\gamma_5$, $t_{\rm flow} = r_{17}10^{17}$ cm/c, we find that for IR-emitting particles, $\eta_{\rm IR} = 0.05\gamma_5^3 B_{-3}^{-3/2} r_{17}^{-1}$, and $\dot{N}_{\rm IR} = 2\times10^{36}\gamma_5^2 B_{-3}^{-1} r_{17}^{-1}$ s^{-1} sr^{-1}. The spectral index of the knot indicates that the particle distribution power-law index should be $p \sim 2.6$, thus the IR-emitting particles should comprise the majority of particle pressure downstream. From the above estimations, it seems that the particle injection rate at the shock is marginally consistent with the scenario that most of the IR/optical-emitting particles are provided by the shock.

Regarding particle acceleration mechanisms, we notice that IR-emitting particles usually go through $N = t_{\rm flow}\nu_g$ Larmor orbits, where $\nu_g = \nu_B/\gamma'$ is the relativistic gyrofrequency—the cyclotron frequency (ν_B) divided by the electron's Lorentz factor (γ'). Eliminating γ' in favor of the magnetic field (B) and observing frequency (ν), the number of orbits within the flow timescale is $N \approx 6\times10^4 B_{-3}^{3/2} r_{17}\nu_{14}^{-1/2}$. To allow sufficient time for acceleration mechanisms requiring instabilities or stochastic processes to operate, requires that $N >> 1$. However, for particles emitting γ rays of energy 300 MeV, $N \lesssim 1$, thus requiring special acceleration mechanisms—if the emitting electrons are indeed accelerated at the shock.

One more constraint comes from the polarization of the knot. Most recent polarimetry performed by Moran et al. (2013) gives a high polarization degree of ~60%, with position angle aligned with the symmetry axis, indicating a strongly toroidal magnetic field. Here we need to be careful about the depolarization effect due to relativistic kinematics (Lyutikov et al. 2003). What happens then is that Lorentz transformation of the emission of a relativistic plasma from the comoving frame to the lab frame produces a rotation of the polarization vector. For a curved emitting surface, neighboring fluid elements have slightly different velocities, thus their polarization vectors experience different amounts of rotation. As one sums the contribution from the visible surface (this is essentially what we observe), the result is some degree of depolarization. We find that for the oblique shock in the Crab Nebula, under an ultrarelativistic approximation, the upper limit of polarization degree is similar to that in Lyutikov et al. (2003): 56.25% for particle spectral index $p = 3$ and 43.4% for $p = 2$. Thus, the observed high degree of polarization and its possible variation are highly constraining on theoretical models. Mildly relativistic outflow may give a higher polarization degree but may not produce a small enough knot (see Porth et al. 2014). In addition, particle acceleration mechanisms that generate turbulence could further depolarize the emission. It would be interesting to repeat this polarization observation, especially with AO.

7. CONCLUSIONS

We have (1) introduced a new approach for analyzing time series images; (2) discovered that the key properties of the knot (radial width, tangential width, flux) are correlated with the time-variable separation between the knot and the pulsar; (3) shown that with the available data it is not possible to determine a strong correlation between the knot separation and the occurrence of γ-ray flares; (4) set an upper limit to the low-energy X-ray flux from the inner knot; and (5) discussed the implications of our observations to set constraints on particular elements of the standard shock modeling of the relativistic outflow from the pulsar. These include inferences as to wind magnetization σ, shock shape parameters such as incident angle δ_1, and poloidal radius of curvature R_c, as well as the IR/optical-emitting particle enthalpy fraction. We found that while the standard shock model gives good agreements with observations in many aspects, there remain two puzzles: (a) the angular size of the knot relative to the pulsar–knot separation is much smaller than expected; and (b) the variable yet high degree of polarization is difficult to reconcile with a highly relativistic outflow (see, however, Porth et al. 2014). We also found that the IR/optical flux of the inner knot is marginally consistent with the scenario in which the shock accelerates most of the optical-emitting particles in the nebula.

The *Fermi*/LAT Collaboration acknowledges generous ongoing support from a number of agencies and institutes that have supported both the development and the operation of the LAT as well as scientific data analysis. These include the National Aeronautics and Space Administration and the Department of Energy in the United States, the Commissariat à l'Energie Atomique and the Centre National de la Recherche Scientifique/Institut National de Physique Nucléaire et de Physique des Particules in France, the Agenzia Spaziale Italiana and the Istituto Nazionale di Fisica Nucleare in Italy, the Ministry of Education, Culture, Sports, Science, and Technology (MEXT), High Energy Accelerator Research Organization (KEK), and the Japan Aerospace Exploration Agency (JAXA) in Japan, and the K. A. Wallenberg Foundation, the Swedish Research Council, and the Swedish National Space Board in Sweden. Additional support for science analysis during the operations phase is gratefully acknowledged from the Istituto Nazionale di Astrofisica and the Centre d'Etudes Spatiales in France. The research leading to these results has also received funding from the European Commission Seventh Framework Programme (FP7/2007-2013) under grant agreement n. 267251. Several of the authors would also like to acknowledge both funding and solid support from the *Chandra* X-ray Center and the *Hubble Space Telescope* Science Institute under a number of observing proposals: GO3-14054Z, GO3-14057Z, GO4-15058Z, GO4-15059Z, GO-13109, GO-13196, and GO-13348.

APPENDIX
DATA ANALYSIS

A.1. Keck

To study the knot using the high-resolution Keck adaptive optics (AO) data, we characterize the region around the pulsar using an empirically measured PSF and an analytical model of the knot geometry.

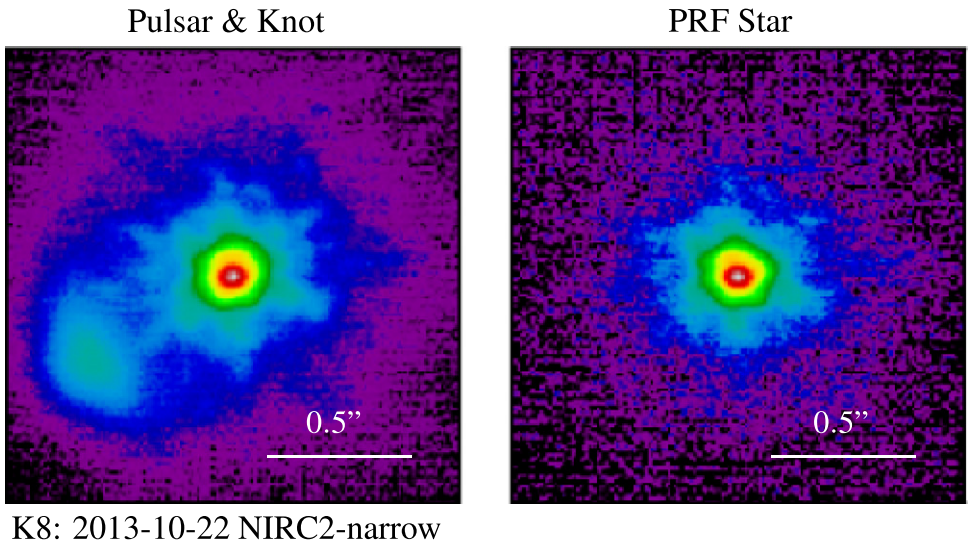

Figure 11. Pulsar (left) and a nearby star (right) from Keck data taken on 2013 October 22. (a) An *H* filter image of the pulsar and knot (in the lower-left) as seen by the NIRC2-narrow camera (0.″01 pixels and a 10″ × 10″ field of view). The structure of the knot is resolved and separated from the pulsar by a statistically significant valley. (b) A nearby (5″) comparison star, used to establish the point-response-function. Both images are shown with a logarithmic color stretch.

Table 10
Results of the Traditional Analysis of the First 17 *HST* Observations

#	r_0 ″	FWRMS$_r$ ″	FWRMS$_t$ ″	F_k e/s
H1	0.660 ± 0.012	0.287 ± 0.019	0.551 ± 0.037	116.5 ± 2.9
H2	0.634 ± 0.012	0.283 ± 0.020	0.538 ± 0.038	110.9 ± 2.8
H3	0.649 ± 0.013	0.333 ± 0.021	0.594 ± 0.038	131.6 ± 3.3
H4	0.615 ± 0.012	0.255 ± 0.020	0.489 ± 0.038	90.4 ± 2.3
H5	0.588 ± 0.012	0.278 ± 0.019	0.560 ± 0.038	112.9 ± 2.8
H6	0.635 ± 0.012	0.290 ± 0.020	0.552 ± 0.037	111.6 ± 2.8
H7	0.706 ± 0.010	0.288 ± 0.021	0.589 ± 0.044	97.6 ± 2.4
H8	0.734 ± 0.017	0.336 ± 0.024	0.658 ± 0.046	109.2 ± 2.7
H9	0.732 ± 0.013	0.319 ± 0.022	0.650 ± 0.046	108.1 ± 2.7
H10	0.641 ± 0.009	0.299 ± 0.020	0.580 ± 0.039	117.6 ± 2.9
H11	0.637 ± 0.011	0.314 ± 0.020	0.561 ± 0.036	129.2 ± 3.2
H12	0.613 ± 0.012	0.258 ± 0.017	0.578 ± 0.039	121.3 ± 3.0
H13	0.547 ± 0.009	0.224 ± 0.015	0.491 ± 0.033	119.2 ± 3.0
H14	0.552 ± 0.009	0.236 ± 0.015	0.511 ± 0.033	124.8 ± 3.1
H15	0.631 ± 0.012	0.268 ± 0.018	0.588 ± 0.040	115.2 ± 2.9
H16	0.614 ± 0.011	0.266 ± 0.025	0.519 ± 0.049	116.9 ± 2.9
H17	0.624 ± 0.012	0.259 ± 0.024	0.549 ± 0.050	127.8 ± 3.2

A.1.1. PSF Subtraction

We subtracted the PSF of the pulsar using a nearby PSF star (Figure 11). During our observations, the laser guide star, and thus the center of the anisoplanatic patch, was aimed at the point halfway between the PSF star and the pulsar. We fit the PSF star, a background plus a power-law based seeing-disk, to the pulsar. For the fit, we excluded the region in the pulsar sub-image that surrounds the knot and used the other 270°. The background was fit with a sloping plane model to allow for the variable nebular background in the pulsar and PSF star sub-images. The fitting was performed with a Levenburg–Marquadt fitter.

A.1.2. Deconvolution

We chose not to deconvolve the knot with the empirically measured PSF. Tests on several images showed that deconvolution of the shape of the knot made insignificant differences to the fit values and uncertainty.

Table 11
Results of Regression Analyses for the First 17 *HST* Observations Based on the Traditional Data Analysis

Power-law for $r_1 = 0.''6342$				
Property	Unit	$p(r_1)$	Power-law Index q	Probability
FWRMS$_r$	″	0.2801 ± 0.0046	1.14 ± 0.21	6.0E-5
FWRMS$_t$	″	0.5605 ± 0.0067	0.85 ± 0.15	4.9E-5
F_k	e/s	114.8 ± 2.6	−0.39 ± 0.29	1.9E-1

A.1.3. Knot Model

To fit the geometric parameters of the knot, we masked out the center diffraction-limited core of the pulsar, and used a Levenburg–Marquadt fitting technique to fit a two-dimensional Gaussian to the shape of the Knot.

We used a model of the form $S(r, \psi) = S_b + S_k \exp\left(-\frac{1}{2}\left((r - r_0)^2/\sigma_r^2 + (\psi - \psi_0)^2/\sigma_\psi^2\right)\right)$.

We also allowed the center of the coordinate system (x_0, y_0) to vary slightly (0.″05). To determine the fit uncertainties, we used the 1σ errors from the self-covariance of the fit parameters. Results were tabulated in Table 4.

A.2. HST

A.2.1. HST—*Traditional Analysis*

In order to measure the knot properties (position, flux, tangential, and radial width) we used the SExtractor package (Bertin & Arnouts 1996). SExtractor has been extensively used for the analysis of *HST* data, in particular for the ACS camera (e.g., for the *Hubble* Ultra Deep Field project, Beckwith et al. 2006). For source detection, we require a minimum of five contiguous pixels with a detection threshold 5σ above the rms background, with a total of 32 deblending subthresholds, and

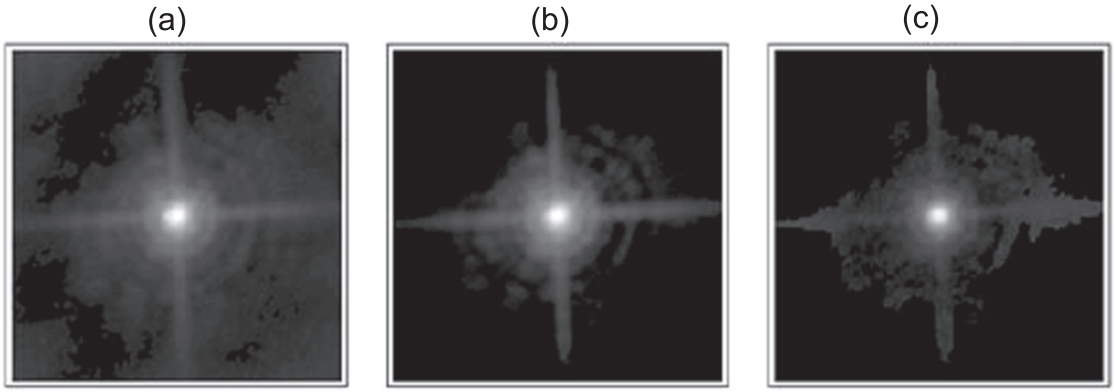

Figure 12. Images illustrating the steps in determining the *HST*/ACS PSF for this analysis: (a) extract 418 (19 × 22) 121 × 121 pixel (6.″05 × 6.″05) images and subtract a linear-gradient background for 19 isolated stars in these 22 *HST*/ACS observations of the Crab; (b) register images of stars and use singular-value decomposition (SVD) to determine a basis describing the PSF (first SVD component shown); and (c) model the pulsar image using the first 72 SVD components.

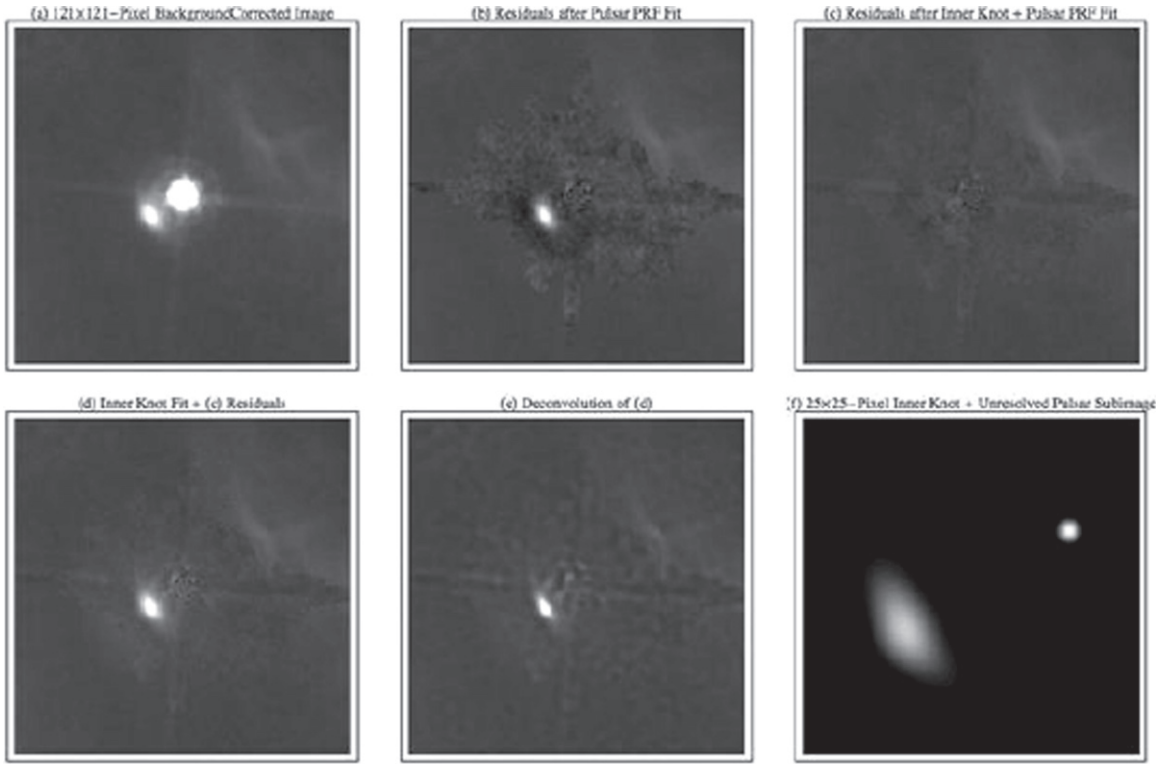

Figure 13. Images further illustrating steps in processing *HST*/ACS images of the Crab pulsar and inner knot: (a) subtract a linear-gradient background in the central 121 × 121 pixel (6.″05 × 6.″05) image of the pulsar and inner knot; (b) remove the pulsar using SVD model of PSF leaving inner knot; (c) remove the inner knot using its SVD model leaving residual background; (d) add the SVD model of the inner knot to the residual background; (e) apply the Richardson–Lucy algorithm to generate a deconvolved image of the inner knot (and residual background); and (f) synthesize the 25 × 25 pixel (1.″25 × 1.″25) sub-image of the registered (unresolved) pulsar and SVD model of the inner knot.

with a contrast parameter of 0.005, setting the background mesh size to 16 × 16 ACS pixels.

The position of a source is evaluated by SExtractor as the barycenter of the source brightness distribution. Flux is computed within an elliptical aperture, using an implementation of the method by Kron (1980). Note that the pulsar is not saturated and that diffraction spikes from the pulsar that might cross the inner knot only marginally affect its flux measurements. The parameters of this ellipse (semiaxes and orientation), evaluated using the second moments of the object's brightness distribution also yield a measure of the object morphology. Indeed, for the case of the knot, the direction of the minor axis of the ellipse turned out to be consistent with the pulsar–knot direction in all images. Thus, the minor axis and the major axis of the ellipse measure the rms full widths (FWRMS) in the radial and tangential directions, respectively.

In order to assess systematic errors, we performed simulations with the ESO/MIDAS software.[13] We added to the ACS images a "synthetic knot." To generate such an artificial source, we assumed a two-dimensional Gaussian brightness distribution, with the minor axis aligned with the true pulsar–knot direction. The synthetic knot was positioned to the NW of the

[13] https://www.eso.org/sci/software/esomidas/

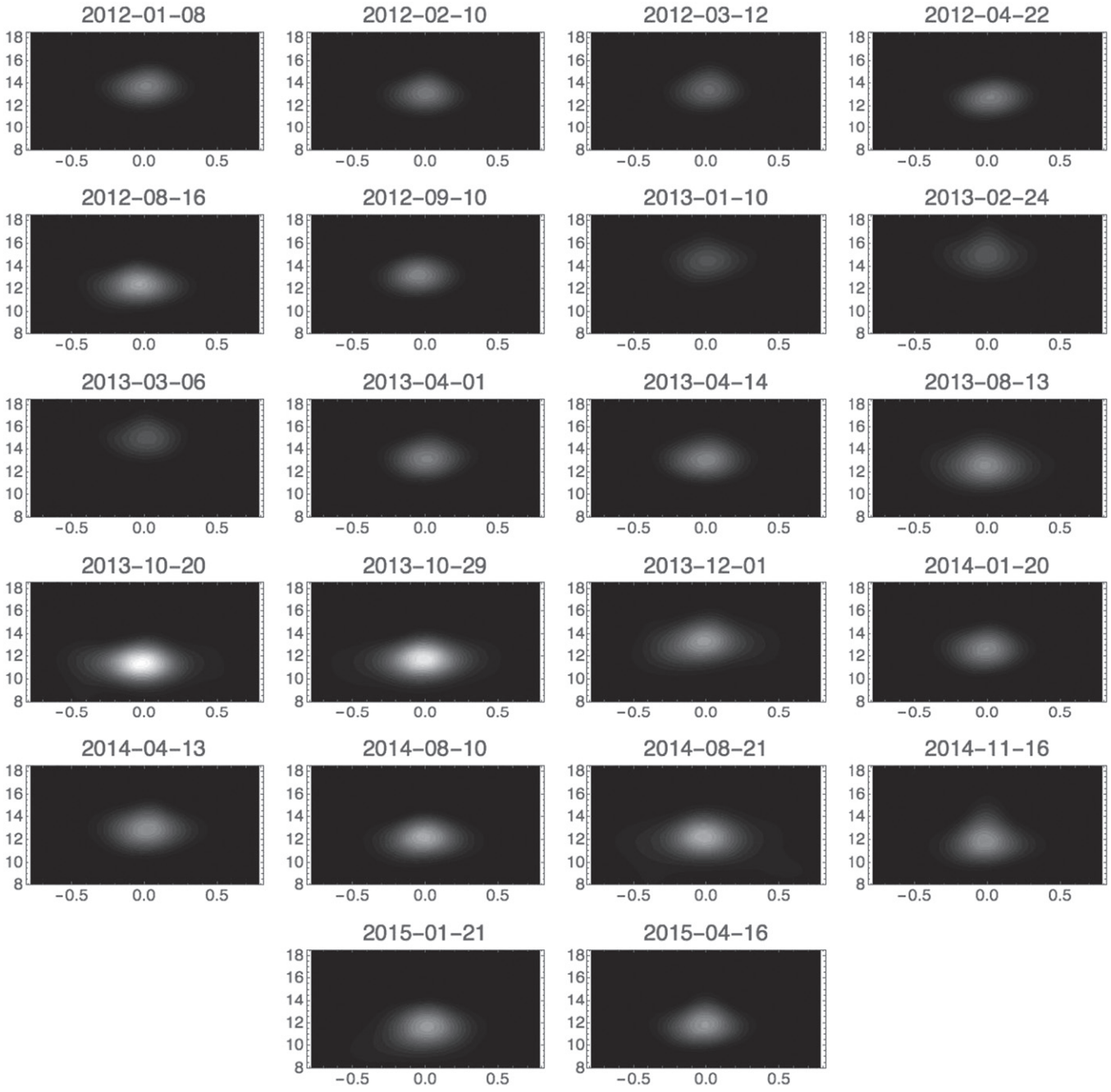

Figure 14. Mapping of processed images of the inner knot onto a ψ–r grid. Here ψ is the angular displacement in radians from the knot's centroid; r, the radial distance from the pulsar in ($0\farcs05$) pixels.

pulsar, opposite but along the true pulsar–knot direction, and at an angular distance comparable to that of the true knot. We repeated the exercise by varying the flux, position, and morphology of the synthetic knot and we estimated the uncertainties in the parameters recovered using SExtractor.[14]

Table 10 lists the best-fit values of the model parameters of the inner knot for each of the first 17 observations based upon this traditional analysis and modeling. Table 11 shows the results of a regression analysis on the listed parameters. We obtained an additional five *HST* observations but did not perform the traditional analysis on those data.

[14] http://www.astromatic.net/software/sextractor

A.2.2. HST-*SVD*

As the inner knot is within $1''$ of the Crab pulsar and varies in position and size, we also developed special procedures for characterizing it using the central 121 × 121 pixel ($6\farcs05 \times 6\farcs05$) images of the 22 *HST*/ACS observations. The major steps are (1) to remove the pulsar from each image, (2) to use the residual image to generate an image of the inner knot, and (3) to characterize the properties of the inner knot.

A.2.2.1. Remove the Pulsar and Generate an Image

In order to remove the pulsar from each of the 22 central 121 × 121 pixel ($6\farcs05 \times 6\farcs05$) *HST* images, we first

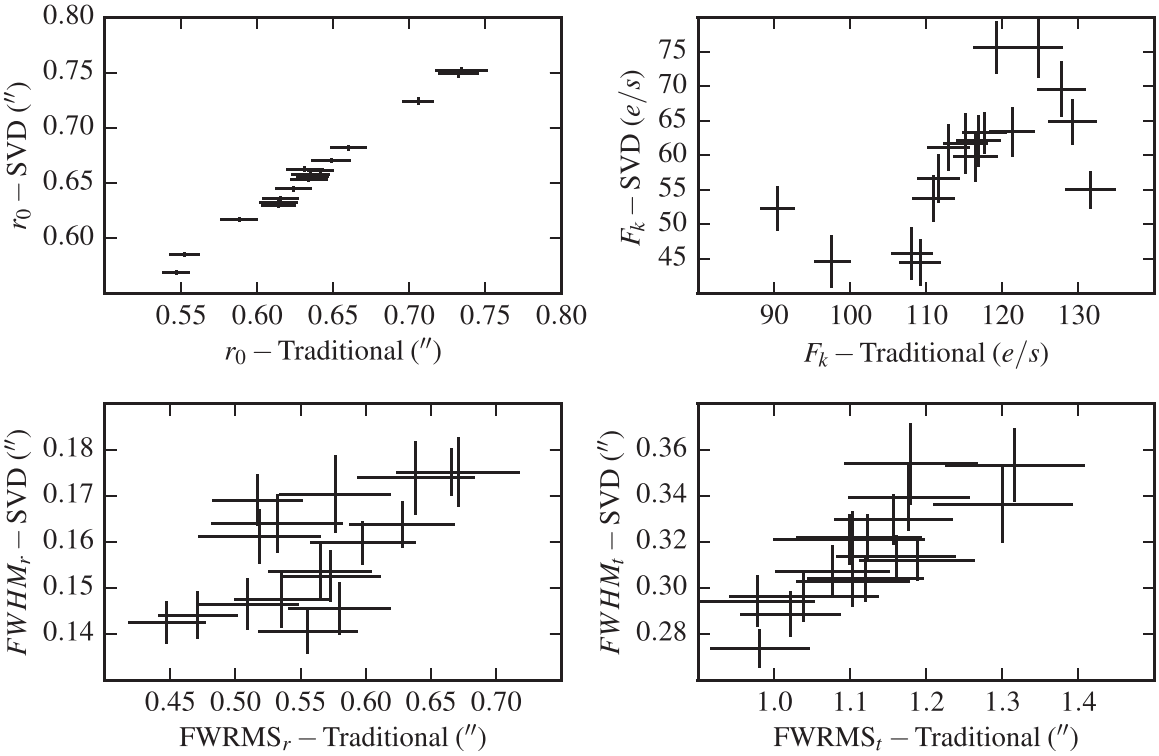

Figure 15. Comparison of *HST*-SVD and *HST*-traditional measured properties of the inner knot.

determine the PSF of the *HST*/ACS using 121 × 121 pixel images around each of the 19 isolated stars in the field. In doing this, we account for the fact that some observations were at a roll angle ∼180° opposite that of the others. After subtracting a fitted linear gradient from the image of each (Figure 12) of the 19 stars and for each of the 22 observations, we register the resulting 418 = 19 × 22 star images and use SVD to generate a linear basis (lowest term shown in Figure 12) describing the PSF. The model pulsar image (Figure 12) uses the first 72 components of the SVD basis. After subtracting a linear gradient from each of the 22 central (pulsar) images (Figure 13), we fit each using the PSF basis to generate 22 residual (pulsar removed) images (also Figure 13), each now dominated by the inner knot.

A.2.2.2. Characterize Inner-knot Properties

The measured extrinsic properties of the inner knot are the projected radial separation r_0 and the polar angle ψ_0 of the peak surface brightness with respect to the pulsar. To facilitate characterization of the intrinsic properties of the inner knot, we map each inner knot sub-image (Figure 13) onto a ψ–r grid (Figure 14). For an initial model of the surface brightness (intensity) distribution of the inner knot, we use a simple bivariate normal distribution: $S(r, \psi) = S_{\rm k} \exp(-\frac{1}{2}((r - r_0)^2/\sigma_r^2 + (\psi - \psi_0)^2/\sigma_\psi^2))$.

The major intrinsic properties of the inner knot are its radial dispersion σ_r (FWHM$_r$ = 2.35σ_r for a Gaussian profile), azimuthal dispersion σ_ψ (or tangential dispersion $\sigma_t = r_0\sigma_\psi$), and peak intensity (surface brightness) $S_{\rm k}$. Integrating the intensity over a solid angle gives the flux $F_{\rm k} = 2\pi\sigma_r\sigma_t S_{\rm k}$. In fitting this model to the ψ–r image of the inner knot, we include a constant-surface-brightness background $S_{\rm b}$ as a model parameter.

While this simple model provides adequate estimates to characterize the primary properties of the knot (Table 6), as a check we also introduced a somewhat more complicated model to deal with minor asymmetries in the ψ–r plane. In particular, we took the radial location and radial width to be weak functions of the azimuthal angle, which we expand as a Taylor series to second order: $r \approx r(\psi) \approx r_0 + r_0'(\psi - \psi_0) + \frac{1}{2}r_0''(\psi - \psi_0)^2$ and $\sigma_r \approx \sigma_r(\psi) \approx \sigma_{r_0} + \sigma_{r_0}'(\psi - \psi_0) + \frac{1}{2}\sigma_{r_0}''(\psi - \psi_0)^2$. However, the derivatives proved not to significantly alter the results.

A.2.2.3. Comparison Between Methods

The comparison between methods and the reasons for somewhat emphasizing the SVD-based results considers the various measured parameters individually. Figure 15 compares measurements of similar variables between the two methods. From the figure we see that with the possible exception of the knot flux, both methods yield measurements that track each other apart from a scale factor. This leads to the result that the pulsar–knot separation determines all of the intrinsic properties of the knot.

Differences for r_0 are quite small, whereas the knot flux and size estimates differ by factors of ≈2. We would expect differences in the size estimates, as the two analyses are using different measures of knot size—the first, FWRMS; the second, FWHM—that are not simply related for a non-Gaussian profile. That the fluxes differ is perhaps not so surprising, as its measurement is sensitive to the method of background subtraction and the impact of emission in the wings of the inner knot's profile. A significant difference between the two methods is the smaller uncertainty in r_0 afforded by the SVD approach, which removes those SVD components that represent noise, thus enhancing signal to noise.

A.3. Chandra

Figure 6 shows the summed image at pulse minimum from the six "flaring" observations (ObsIDs 14684-16247 in Table 3). Prior to the binning used to produce the figure, we extract the counts in the three regions shown. It is difficult, if not impossible, to make use of the absolute number of counts as the different instrument configurations are all uncalibrated. However, we can make use of the relative numbers of counts from the different regions. Thus, the central region serves as an indicator of the number of pulsar counts, which can then be compared with the other observations to derive physical fluxes (assuming of course that the phase-averaged pulsar flux has not varied). The region to the southeast provides the upper limit for the flux in the knot and we use the region to the northwest to estimate the background, comprised mainly of that due to the wings of the pulsar PSF.

The alert reader will notice a slight excess of counts roughly $0\farcs6$ to the southwest of the pulsar. This feature is seen both in the phase-averaged pulse and in the data from ObsID 11245. (The asymmetric effect of the blade inserted for ObsID 9765 does not allow these data to be used in making this comparison.) Therefore, we conclude that this feature is part of the pulsar PSF. A more subtle effect is also present as there is a slight asymmetry in the PSF that causes the region we associate with the inner knot to be somewhat brighter than the background during observations taken in the fall. In the spring, when the spacecraft has (naturally) been set at a roll angle that differs by $\approx 180^\circ$ from that in the fall, the background region is brighter than that we associate with the location of the inner knot. This effect is mainly seen in the phase-averaged data, and by comparing data from the ObsID 9765 (spring) and ObsID 11245 (fall) observations. Both effects described in this paragraph are relatively minor and are mainly due to the fact that we are working slightly below the spatial resolution of *Chandra*; thus, these effects have been ignored in setting the upper limits in Table 8.

REFERENCES

Aliu, E., Archambault, S., Aune, T., et al. 2014, ApJL, 781, LL11
Arons, J. 2012, SSRv, 173, 341
Baty, H., Petri, J., & Zenitani, S. 2013, MNRAS, 436, L20
Beckwith, S. V. W., Stiavelli, M., Koekemoer, A. M., et al. 2006, AJ, 132, 1729
Bertin, E., & Arnouts, S. 1996, A&AS, 117, 393
Bogovalov, S. V. 1999, A&A, 349, 1017
Buehler, R., Scargle, J. D., Blandford, R. D., et al. 2012, ApJ, 749, 26
Bühler, R., & Blandford, R. 2014, RPPh, 77, 066901
Buson, S., Buehler, R., & Hays, E. 2013, ATel, 5485, 1
Bykov, A. M., Pavlov, G. G., Artemyev, A. V., & Uvarov, Y. A. 2012, MNRAS, 421, L67
Camus, N. F., Komissarov, S. S., Bucciantini, N., & Hughes, P. A. 2009, MNRAS, 400, 1241
Cerutti, B., Uzdensky, D. A., & Begelman, M. C. 2012, ApJ, 746, 148
Cerutti, B., Werner, G. R., Uzdensky, D. A., & Begelman, M. C. 2013, ApJ, 770, 147
Clausen-Brown, E., & Lyutikov, M. 2012, MNRAS, 426, 1374
Fitzpatrick, E. L. 1999, PASP, 111, 63
Fruchter, A. S., & Hook, R. N. 2002, PASP, 114, 144
Ghez, A. M., Salim, S., Weinberg, N. N., et al. 2008, ApJ, 689, 1044
H. E. S. S. Collaboration Abramowski, A., Aharonian, F., et al. 2014, A&A, 562, A145
Hester, J. J. 2008, ARA&A, 46, 127
Hester, J. J., Scowen, P. A., Sankrit, R., et al. 1995, ApJ, 448, 240
Komissarov, S. S., & Lyubarsky, Y. E. 2003, MNRAS, 344, L93
Komissarov, S. S., & Lyutikov, M. 2011, MNRAS, 414, 2017
Kron, R. G. 1980, ApJS, 43, 305
Lyubarsky, Y. E. 2012, MNRAS, 427, 1497
Lyutikov, M., Balsara, D., & Matthews, C. 2012, MNRAS, 422, 3118
Lyutikov, M., Pariev, V. I., & Blandford, R. D. 2003, ApJ, 597, 998
Mayer, M., Buehler, R., Hays, E., et al. 2013, ApJL, 775, L37
Melatos, A., Scheltus, D., Whiting, M. T., et al. 2005, ApJ, 633, 931
Moran, P., Shearer, A., Mignani, R. P., et al. 2013, MNRAS, 433, 2564
Ng, C.-Y., & Romani, R. W. 2008, ApJ, 673, 411
Ojha, R., Hays, E., Buehler, R., & Dutka, M. 2013, ATel, 4855, 1
Porth, O., Komissarov, S. S., & Keppens, R. 2014, MNRAS, 438, 278
Rees, M. J., & Gunn, J. E. 1974, MNRAS, 167, 1
Sandberg, A., & Sollerman, J. 2009, A&A, 504, 525
Sollerman, J. 2003, A&A, 406, 639
Sollerman, J., Lundqvist, P., Lindler, D., et al. 2000, ApJ, 537, 861
Striani, E., Tavani, M., Piano, G., et al. 2011, ApJL, 741, L5
Sturrock, P., & Aschwanden, M. J. 2012, ApJL, 751, L32
Tavani, M., Bulgarelli, A., Vittorini, V., et al. 2011, Sci, 331, 736
Tchekhovskoy, A., Philippov, A., & Spitkovsky, A. 2015, arXiv:1503.01467
Tchekhovskoy, A., Spitkovsky, A., & Li, J. G. 2013, MNRAS, 435, L1
Tennant, A. F., Becker, W., Juda, M., et al. 2001, ApJL, 554, L173
Teraki, Y., & Takahara, F. 2013, ApJ, 763, 131
Tziamtzis, A., Lundqvist, P., & Djupvik, A. A. 2009, A&A, 508, 221
Uzdensky, D. A., Cerutti, B., & Begelman, M. C. 2011, ApJL, 737, L40
Weisskopf, M. C., Tennant, A. F., Arons, J., et al. 2013, ApJ, 765, 56
Wizinowich, P. L., Le Mignant, D., Bouchez, A. H., et al. 2006, PASP, 118, 297
Yelda, S., Lu, J. R., Ghez, A. M., et al. 2010, ApJ, 725, 331
Yuan, Q., Yin, P.-F., Wu, X.-F., et al. 2011, ApJL, 730, L15